A numerical solver for coupled dynamic simulation of glacial ice impacts considering hydrodynamic-ice-structure interaction

Zhaolong Yu [a,b,*], Jørgen Amdahl [a,b]

[a] Department of Marine Technology, Norwegian University of Science and Technology (NTNU), Norway
[b] Center for Autonomous Marine Operations and Systems (AMOS), Norwegian University of Science and Technology (NTNU), Norway

ARTICLE INFO

ABSTRACT

Glacial ice features pose great threats on the safety of ships and offshore structures in the arctic. House sized bergy bits or growlers are of particular concern because of the detection capability limits of marine radars. Analysis and design of structures against collisions from such glacial ice bodies has always been challenging due to the complicated hydrodynamic-ice-structure interaction.

This paper proposes a numerical solver for coupled simulation of glacial ice impacts accounting for the effects of hydrodynamic-ice-structure interaction. The solver adopts user subroutines provided in LS-DYNA and combines three different modules, i.e. the BWH (Bressan-Williams-Hill) criterion for the prediction of fracture of steels, a hydrostatic pressure dependent plasticity-based material model for constitutive modelling of ice, and the linear potential flow theory for hydrodynamic loads.

The proposed solver is verified and calibrated to ice resistance data from field tests and is then applied to simulate ice collisions on a semi-submersible platform column. Collision scenarios with both in-plane 3DOF and full 6DOF ice motions are considered. The results are discussed with respect to ice motion trajectories, ice crushing and structural damage under the combined action of ice indentation and sliding loads. The dissipated energy predicted by external dynamic models is compared with simulation results and discussed.

1. Introduction

Human activities increase continuously in the Arctic regions related to exploration and production of natural resources (e.g. oil and gas) and maritime shipping. This raises great concern on the safe operation of ships and offshore platforms in ice infested waters. Potential impacts from glacial ice may cause significant structural damage, leading to economic loss, environmental polution and in the extreme cases, fatalities and progressive collapse of structures. It is therefore crucial to understand the mechanics of glacial ice impacts and design crashworthy structures to withstand such actions. Relatively small glacial ice features (house sized) are of major concern because they are more difficult to be detected by marine radars and handled by ice management operations, especially in extreme sea states. Fig. 1 shows an example ice feature with a waterline of 30 m moving in waves.

Analysis and design of ships and offshore structures against glacial ice impacts is challenging with multiple interaction effects, including hydrodynamic loads, ice mechanics and structural mechanics. Each of the three requires significant efforts to analyse rationally.

The mechanical behavior of ice during impact is very complicated, and a mature ice material model that describes comprehensively the behavior, is still lacking. A few material models are available in the literature for the constitutive modelling of ice. Gagnon (2011) modelled ice as a crushable foam plasticity material with volumetric hardening. Overlapping mesh layers were adopted to mimic high pressure and low-pressure zones during ice crushing. Ice spalling was simulated by predefined death time of contact between layers. The model was used by Gagnon and Wang (2012) in numerical simulation of a ship-ice collision to estimate damage to the vessel. An alternative is to model ice using elastic-plastic material models with the yield stress dependent on the hydrostatic pressure. Examples are Fish (1991), Derradji-Aouat (2000) and Liu et al. (2011). In addition, Ince et al. (2017a) proposed a constitutive equation for ice materials, associating the failure stress with the effects of strain rate, salinity and temperature. Both ductile and brittle behavior are accounted for according to the level of strain rate. Ice fracture was modelled using a cohesive zone model to define the crack-opening displacement. The ice model was used by Ince et al. (2017b) to reproduce a drop test of ice on a deformable plate. Han et al.
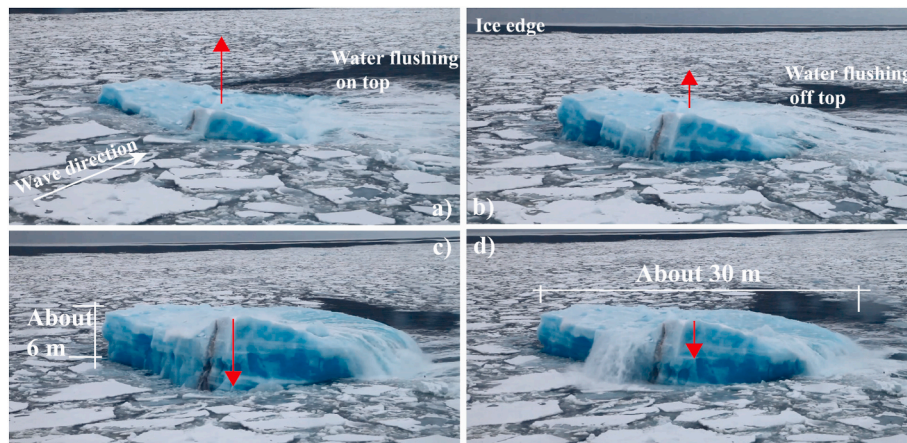

Fig. 1. Motions of a glacial ice feature in waves (filmed by Tsarau A. and Evgenii S. in 2015). From Lu et al. (2020)..
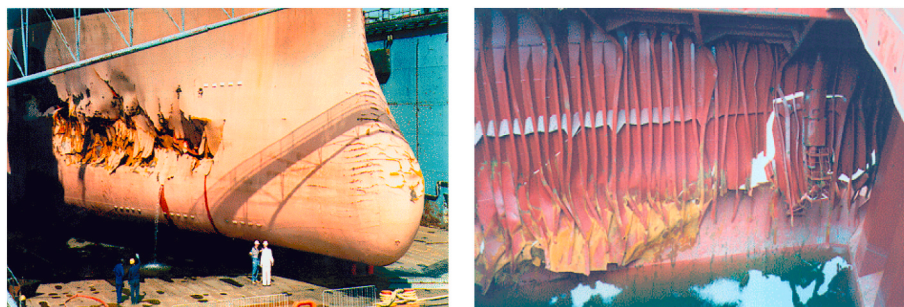

Fig. 2. Structure damage of Reduta Ordona after collision with iceberg, from Hill (2006).

(2017) studied several constitutive ice models and used them to reproduce an ice crushing test.

As regards structural mechanics with nonlinear finite element analysis (NLFEA), it is essential to describe material behavior up to fracture, and correctly calibrate it into theoretical material models. The isotropic power law hardening model with a yield plateau is often used to describe steel behavior. In the structural design stage, often only nominal material properties are provided. The statistical variability of material properties needs to be carefully considered to maintain sufficient margins of structural capacity. In addition, it is still challenging to accurately predict steel fracture initiation and propagation with coarsely meshed shell elements. The complexity lies in the fact that fracture is a very localized phenomenon with a length scale in the range of plate thickness and is difficult to capture with large shell elements that are several times larger than the plate thickness. In addition, ductile fracture of steel depends highly on stress states, loading path and is sensitive to the mesh size adopted (Yu and Amdahl, 2018). Modelling of fracture is, however, crucial for capturing ice structure interaction during glacial ice impact because rupture of side panels may completely change relative strengths of the interacting ice and structure. Quite a few models showed good performance for the prediction of steel fracture modelled with large scale shell elements, e.g. the BWH (Bressan-Williams-Hill) criterion by (Alsos et al., 2008), the RTCL (Rice–Tracey and Cockcroft–Latham) criterion by (Tørnqvist, 2003), etc. The models were validated with various small- and large-scale tests in several benchmark studies, and showed reasonable and consistent predictions in general (Calle et al., 2017; Ehlers et al., 2008; Marinatos and Samuelides, 2015; Storheim et al., 2015).

For hydrodynamic loads during ice impacts, traditional collision analysis often decouples the problem into external dynamics and internal mechanics, and the hydrodynamic effects during collisions are often considered simply as constant added masses for the calculation of dissipated energy in external dynamics. In the assessment of internal mechanics, the striking ice typically moves in a prescribed motion path and hits the structure. The decoupled approach uses the crude assumption of constant added masses for hydrodynamic loads and neglects ice motion effects. The approach was shown to perform with less accuracy for collisions with long durations or significant structural penetration (Yu et al., 2019c). The decoupled method generally works for head-on collisions, which are often considered as the worst condition. This however includes only the indentation type of structural damage. Recent research by Alsos (2008) and Quinton (2008) showed that the structure may be more vulnerable to sliding induced moving loads, which could cause the same structural damage with almost half of the magnitude compared to that by indentation loads alone. An example of the sliding damage is shown in Fig. 2, where the bulk carrier Reduta Ordona was hit by an iceberg and the hull structure was severely damaged as ice slid along.

Proper hydrodynamic modelling is essential to understand the evolution of hydrodynamic loads during collision, the effect of ice motions, and the influence of combined ice indentation and sliding on the structural damage. Computational Fluid Dynamic (CFD) packages are useful tools for the simulation of hydrodynamic loads with high accuracy and significant flow details. The effects of viscosity and multi-body interactions are well included. An example of CFD simulations with application to ice can be found in Huang et al. (2020) using STAR-CCM to calculate ship resistance operating in level ice. CFD simulations, on the other hand, require significant modelling efforts and computational resources, especially when very large fluid domains are involved. It is also challenging to couple CFD simulations with ice material modelling and structural responses. Smoothed Particle Hydrodynamics (SPH) is another potential method to simulate ice structure interactions. SPH employs nodes rather than finite elements, and these nodes may interact through kernel functions, which smooth the properties a set distance
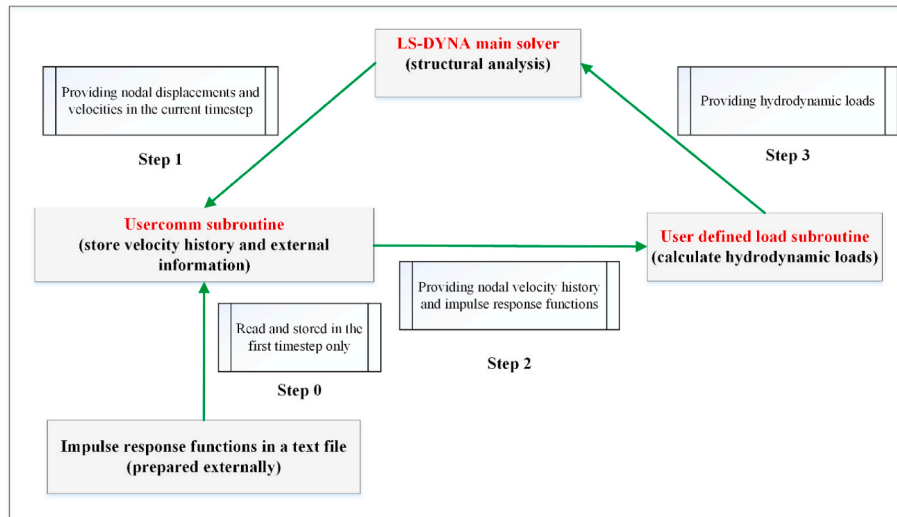
Fig. 3. Illustration of the coupling algorithm.

Table 1
Input parameters for the numerical simulations.

Parameters	Value	References
Ice density (Kg/m^3)	900	ISO 19906 (2010)
Young's Modulus (GPa)	9.5	Timco and Weeks (2010)
Poisson Ratio	0.3	Timco and Weeks (2010)
Ice friction	0.15	Timco and Weeks (2010)
Material coefficient a_0 (MPa^2)	2.588	Kierkegaard (1993)
Material coefficient a_1 (MPa)	8.63	Kierkegaard (1993)
Material coefficient a_2 (−)	−0.163	Kierkegaard (1993)

from the center node. SPH may be used to model both fluids and solids. Examples of SPH applications are Pernas-Sánchez et al. (2012) for the simulation of ice behavior under high speed ice impact and Das and Ehlers (2015) for simulating crushing and bending failure of ice. The Arbitrary Lagrangian Eulerian (ALE) method is a widely used approach to model hydrodynamics during collisions as it is readily available in NLFEA softwares and can be conveniently coupled with structural analysis. In an ALE simulation, the Eulerian mesh is used for modelling the fluid while the Lagrangian mesh is used for the structure. In each

timestep, loads and boundaries are transferred between the structure and fluid. Examples of ALE simulations for ship/ice collisions and water slamming impacts can be found in Song et al. (2016), Gagnon and Wang (2012), Rudan et al. (2019) and Yu et al. (2019a). The ALE method, however, requires significant efforts for modelling and computation, and the results are sensitive to adopted mesh sizes and numerical parameters. Alternatively, the hydrodynamic loads can be modelled based on linear potential flow theory using the MCOL routine in LS-DYNA or the user defined load subroutine in LS-DYNA. MCOL is a 3D external dynamics program for ship collision embedded in LS-DYNA, and examples of applications can be found in Le Sourne et al. (2012) and Kim et al. (2021). Through a user defined load subroutine in LS-DYNA, Yu et al. (2016) and Yu and Amdahl (2016) implemented a traditional maneuvering model and linear potential flow theory, respectively, into LS-DYNA, allowing coupled simulations of ship collisions. The methods are computationally more efficient compared to ALE and CFD simulations and is reasonably accurate.

This paper presents a numerical solver for coupled simulation of glacial ice impacts accounting for hydrodynamic-ice-structure interactions. The solver adopts user subroutines in LS-DYNA and combines three different modules, i.e. the BWH criterion proposed by Alsos et al.
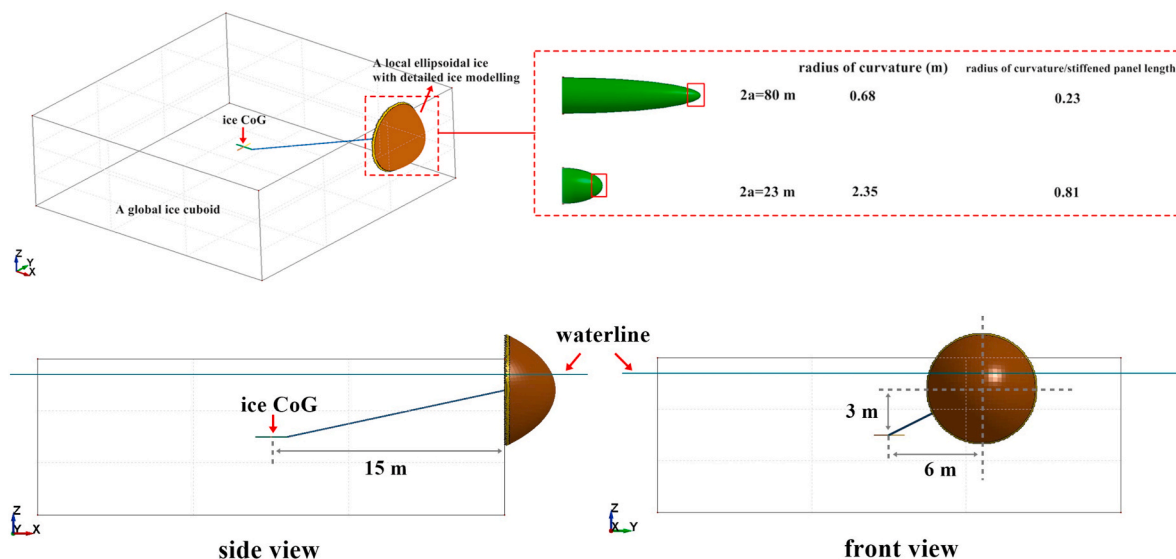

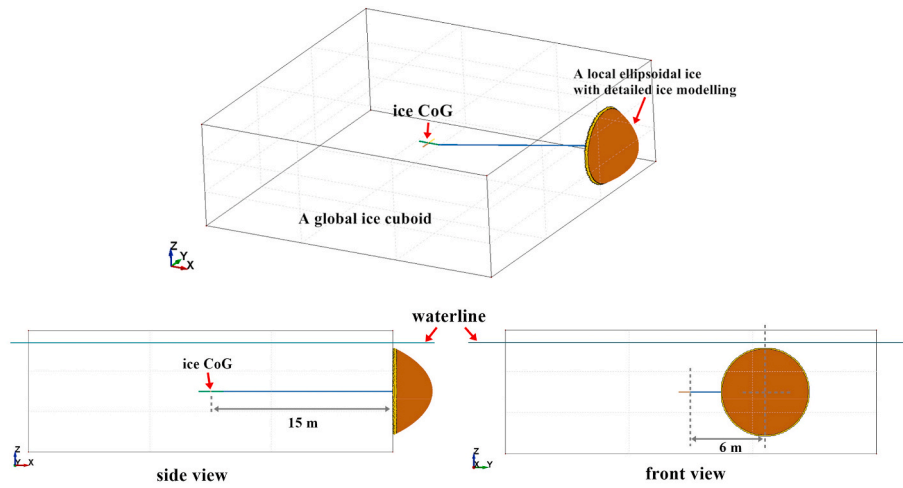**Fig. 4.** The global and local ice geometries for loading Case 1 with both in-plane and out-of-plane eccentricities.

Fig. 5. The global and local ice geometries for loading Case 2 with only in-plane loading eccentricities.

Table 2
Mass and moment of inertia for the ice block.

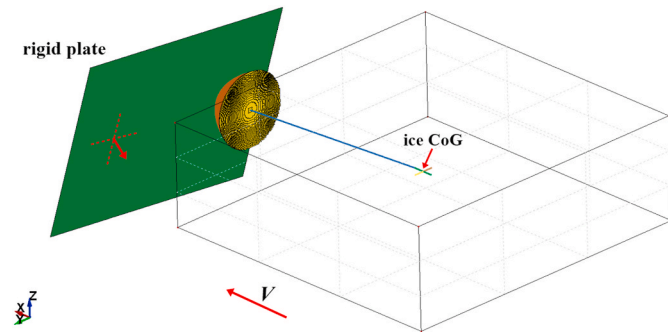|	Total mass (tons)	Moment of inertia I_{xx} (kgm^2)	Moment of inertia I_{yy} (kgm^2)	Moment of inertia I_{zz} (kgm^2)
Properties of the global ice block	8100	1.0×10^9	1.0×10^9	1.4×10^9

Fig. 6. Glacial ice impact on a rigid plate.

(2008) for steel fracture prediction, the material model proposed by Liu et al. (2011) for constitutive modelling of ice, and linear potential flow theory for hydrodynamic loads implemented by Yu et al. (2016) for ship collisions. The proposed solver is used to simulate ice impacts on a semi-submersible platform as an example application, and the results are compared with predictions from external dynamic models. The effects of combined indentation and sliding loads on structural damage are studied and discussed in detail.

2. A numerical solver for glacial ice impact analysis considering hydrodynamic-ice-structure interaction

The coupled numerical solver is developed by adopting user subroutines in the NLFEA software LS-DYNA, where hydrodynamic loads based on linear potential flow theory are implemented with the user defined load subroutine. In addition the user defined material subroutine is adopted for constitutive modelling of the ice material and implementation of the BWH fracture criterion for the steel material.

2.1. Linear potential-flow theory for hydrodynamics

2.1.1. Hydrodynamic loads using linear potential-flow theory

In analogy with ship collision analysis (Yu et al., 2016), it is assumed that before glacial ice impact, the striking ice body is in force equilibrium, where the excitation forces such as current and wave loads are balanced by the hydrodynamic forces acting on the ice, primarily drag forces. Departure from this state due to a sudden change in the external forces causes a change in the hydrodynamic forces acting on the ice (Petersen, 1982). The governing motion equations are:

$$\sum_{k=1}^{6}\left[\left(M_{jk}+A_{jk}(\infty)\right)\ddot{\eta}_k+\int_0^t K_{jk}(t-\tau)\cdot\left[\dot{\eta}_k(\tau)-\dot{\eta}_k(t=0)\right]d\tau\right.$$

$$\left. + C_{jk}\eta_k\right] = F_j(t)(j=1,2,...,6) \tag{1}$$

where M_{jk} , $A_{jk}(\infty)$ and C_{jk} are components of the generalized mass matrix, the added mass matrix at infinite frequency and the restoring matrix of the ice. The index $j=1,...,6$ represents surge, sway, heave, roll, pitch and yaw motion of the ice, respectively. $\dot{\eta}_k(t=0)$ is the velocity component of the striking ice feature in the k_{th} degree of freedom just before impact and $F_j(t)$ is the generalized collision force in the j_{th} degree of freedom. $\int_0^t K(t-\tau)\cdot\dot{\eta}(\tau)d\tau$ is the convolution integral connected with free-surface memory effects and $K_{jk}(t)$ is the so called impulse-response function connected with directions j and k. It provides a radiation load in j direction acting on the ice at the actual time t as a consequence of an impulse speed in k direction experienced by the ice at a previous time instant t-τ. $K_{jk}(t)$ is given alternatively by:

$$K_{jk}(t)=\frac{2}{\pi}\int_0^\infty B_{jk}(\omega)\cos\omega t d\omega=\frac{2}{\pi}\int_0^\infty\left(A_{jk}(\infty)-A_{jk}(\omega)\right)\omega\sin\omega t d\omega \tag{2}$$

$A_{jk}(\omega)$ and $B_{jk}(\omega)$ are the frequency-dependent added mass and linear wave-radiation damping, respectively.

2.1.2. Implementation of the hydrodynamic loads

The user defined load subroutine is adopted for the application of hydrodynamic loads calculated from the linear potential flow theory. The coupling procedure between structural and hydrodynamic solvers is shown in Fig. 3. During simulation, LS-DYNA first passes information of nodal displacements and velocities at the ice center of gravity (CoG) to
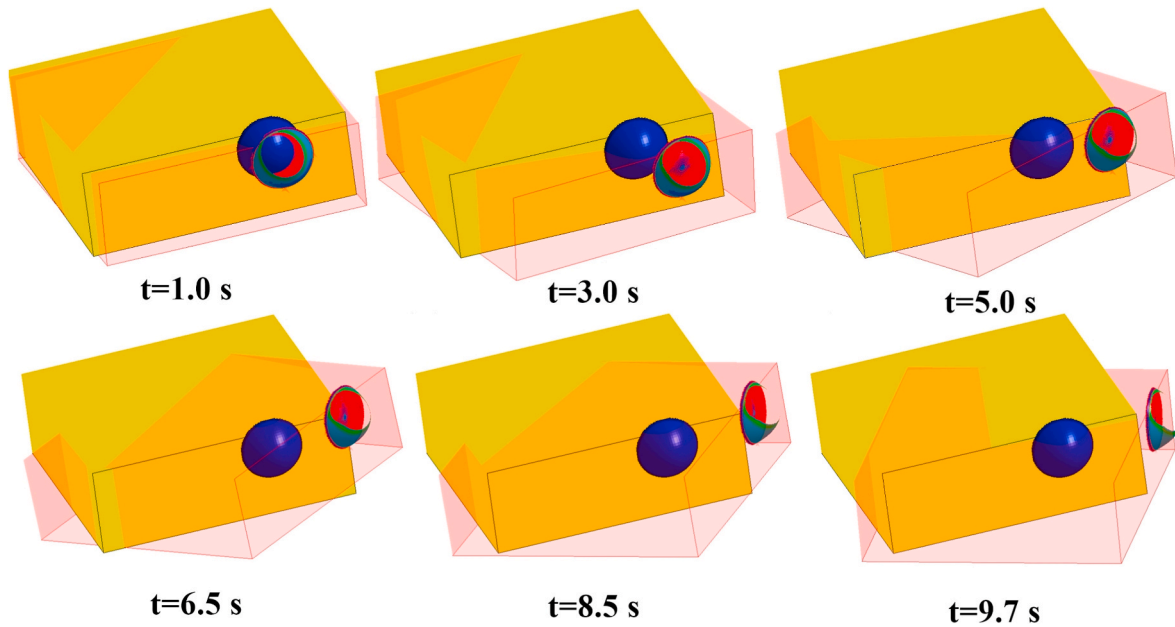
Fig. 7. Snapshots of ice motions during and after collisions. The solid part represents ice configuration at t = 0.0 s and is used as the reference configuration. The transparent part shows the current ice state at different time instants.
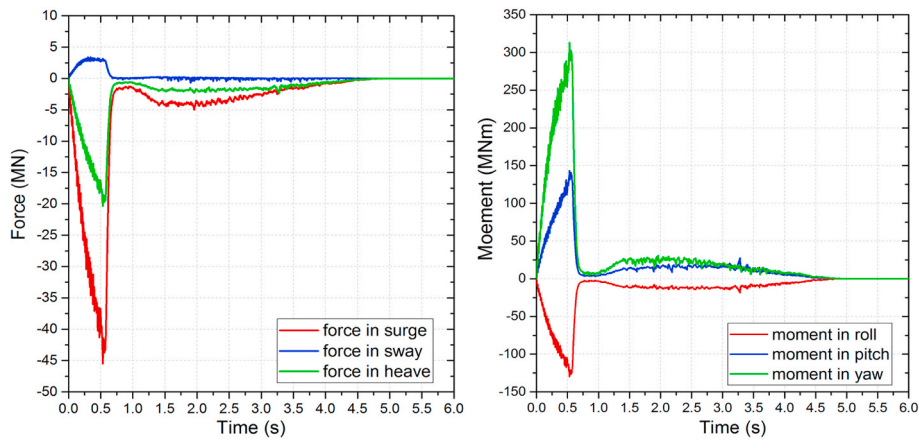

Fig. 8. The collision induced 6DOF forces and bending moments with respect to the ice CoG.

the user subroutine. The velocity history of CoG is then stored in the user common variables. The impulse response functions $K_{jk}(t)$ in the motion equations shall be prepared externally and read and stored in the subroutine in the first timestep. The time increment is typically in the order of 10^{-6} s in ship or ice collision simulation. To maintain efficiency without losing accuracy, the velocity histories are stored every 10^{-3} s. One challenge is that nodal accelerations at CoG are needed in order to apply added mass related forces but are not provided in the subroutine for rigid bodies. Nodal accelerations are recommended to be approximated by the slope of linearly fitted curves of the velocity history data. More details can be found in Yu et al. (2019c).

With the above information, hydrodynamic loads are calculated in the user load subroutine and are applied to the CoG of the ice. LS-DYNA main solver then calculates structural deformation and ice motions and provides information of ice motions for the next timestep.

2.2. An elastic-plastic ice material model

For practical design of structures against abnormal ice loading, we implemented an elastic-plastic material model proposed by Liu et al.

(2011) for constitutive modelling of ice.

The 'Tsai-Wu' elliptic yield criterion given in Eq. (3) is used, where the yield surface is a function of both the second invariant of the deviatoric stress $J_2 = \frac{1}{2} S_{ij} : S_{ij}$ and the hydrostatic pressure $p = -\frac{\sigma_{kk}}{3}$ (pressure positive in compression) to mimic ice confinement,

$$f(p, \ J_2) = J_2 - (a_0 + a_1 p + a_2 p^2) = 0 \tag{3}$$

where, a_1, a_2 and a_3 are material coefficients to be specified by users, and S_{ij} is the deviatoric stress tensor.

To simulate ice failure, an empirical failure criterion is adopted based on the effective plastic strain ε_{eq}^p and the hydrostatic pressure p:

$$\varepsilon_f = \varepsilon_0 + \left(\frac{p}{p_2} - \gamma \right)^2 \tag{4}$$

where, p_2 is the larger root of the yield function, ε_0 and γ are the parameters to be calibrated to ice crushing experiments or target ice properties.

The ice material properties used in the simulation are given in Table 1. The material coefficients a_0, a_1 and a_2 correspond to an ice
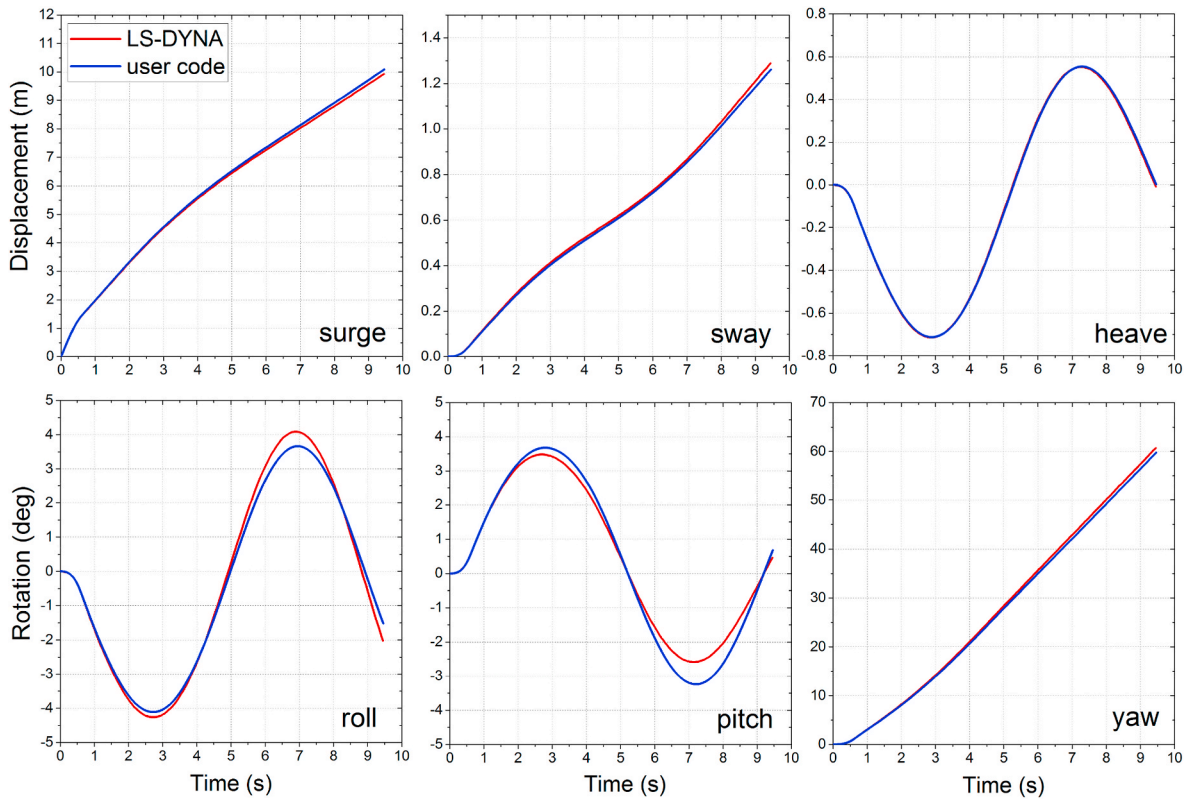
Fig. 9. Comparison of the 6DOF ice motions during and after collision using LS-DYNA and the user code.
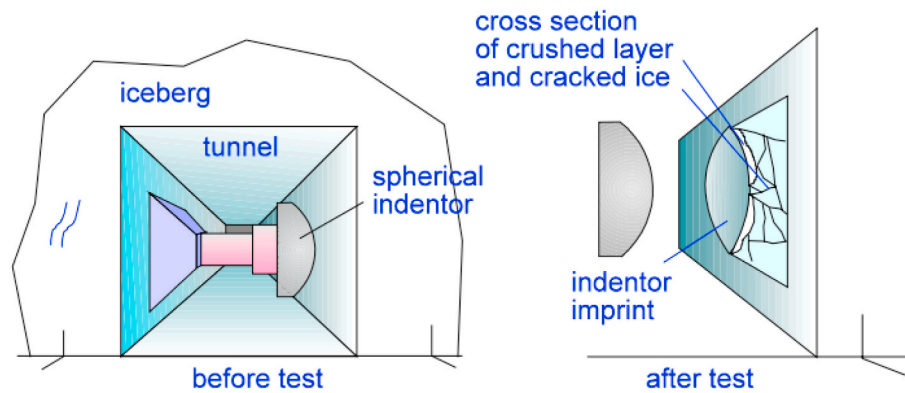

Fig. 10. Arrangement of the Pond Inlet indentation test; picture from Daley (1994).

uniaxial compressive strength of 9.0 MPa and a uniaxial tensile strength of 0.82 MPa.

2.3. The BWH fracture criterion for structural damage

When ice structure interactions are accounted for, proper modelling of the material behavior is essential because the relative strength of the striking ice body and the structure is sensitive to the selected material strength and fracture parameters.

The power law hardening with a yield plateau is used to model the material. The hardening is described by the yield criterion,

$$f = \sigma_{eq} - \sigma_f\left(\varepsilon_{eq}\right) = 0 \tag{5}$$

where σ_{eq} is the von-Mises equivalent stress. The current flow stress σ_f is a function of the equivalent plastic strain ε_{eq} via the power law hardening rule:

$$\sigma_f\left(\varepsilon_{eq}\right) = \begin{cases} \sigma_0 & if \ \varepsilon_{eq} \leq \varepsilon_{plateau} \\ K\left(\varepsilon_{0,eff} + \varepsilon_{eq}\right)^n & if \ \varepsilon_{eq} > \varepsilon_{plateau} \end{cases} \tag{6}$$

where K and n are the hardening parameters and σ_0 is the initial yield stress.

The BWH (Bressan-Williams-Hill) instability criterion is used to model fracture of steel in the ice collision simulation. The criterion, which was proposed by Alsos et al. (2008), combines Hill's local necking model (Hill, 1952) and the shear stress criterion by Bressan and Williams
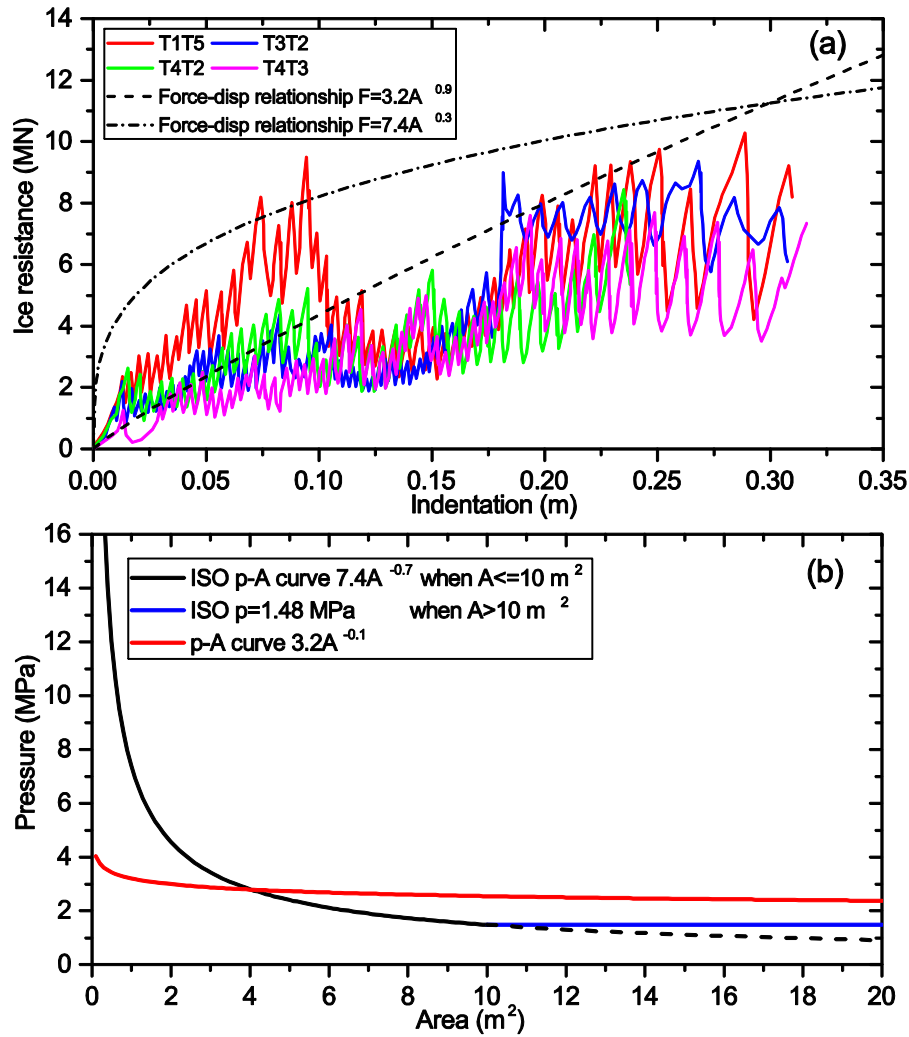
Fig. 11. Force-displacement curves of the Pond Inlet tests (Kennedy, 1990) and (b) Pressure area relationships for the design ice.
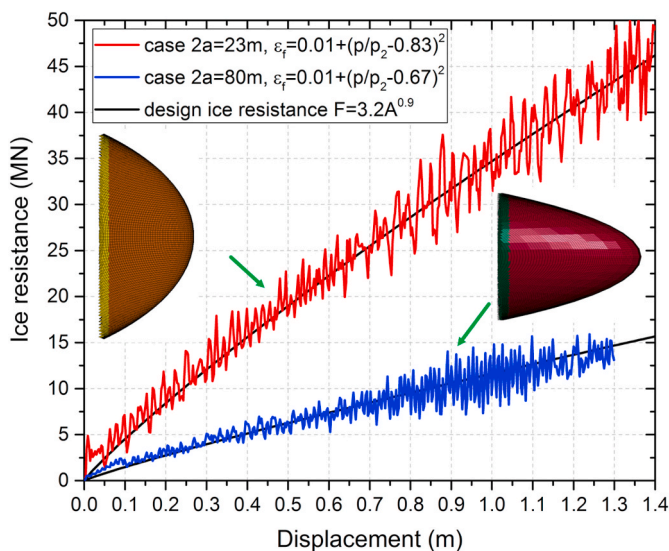

Fig. 12. Case-by-case calibration of ellipsoidal ice with different sharpness.

(1983). It assumes that fracture occurs at the onset of local necking instability neglecting the post-necking regime, which is conservative. It has been validated to be of good accuracy by comparison with various collision experiments (Marinatos and Samuelides, 2015; Storheim et al., 2015). The BWH criterion can be expressed in the principle stress space as follows:

$$
\sigma_1 = \begin{cases} \dfrac{2K}{\sqrt{3}} \dfrac{1+\frac{1}{2}\beta}{\sqrt{\beta^2+\beta+1}} \left(\dfrac{2}{\sqrt{3}} \dfrac{\widehat{\varepsilon}_1}{1+\beta} \sqrt{\beta^2+\beta+1} \right)^n & if \ -1 < \beta \le 0 \\[4ex] \dfrac{2K}{\sqrt{3}} \dfrac{\left(\dfrac{2}{\sqrt{3}} \widehat{\varepsilon}_1 \right)^n}{\sqrt{1-\left(\dfrac{\beta}{2+\beta} \right)^2}} & if \ \ 0 < \beta \le 1 \end{cases}
$$

(7)

β is the ratio of the minor and major principal strain rates, $\beta = \dot{\varepsilon}_2/\dot{\varepsilon}_1$. The critical strain $\widehat{\varepsilon}_1$ can be assumed to be equal to the power law coefficient n in accordance with Hill's criterion.

The BWH fracture criterion is implemented with the user defined material subroutine in LS-DYNA. Fracture is enabled by eroding elements when the criterion is fulfilled. A through-thickness integration point is failed by setting the stresses to zero once the failure criterion is satisfied. Element erosion occurs once the middle integration point fails.
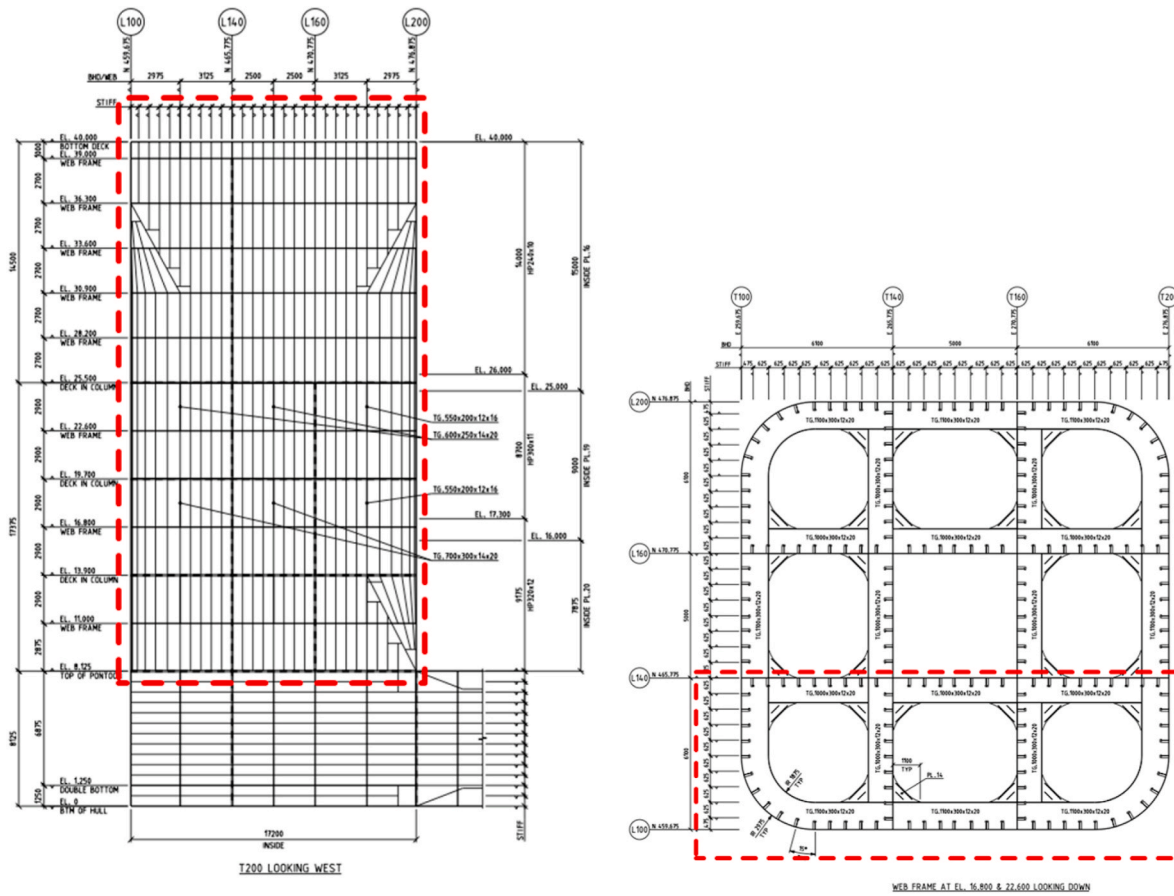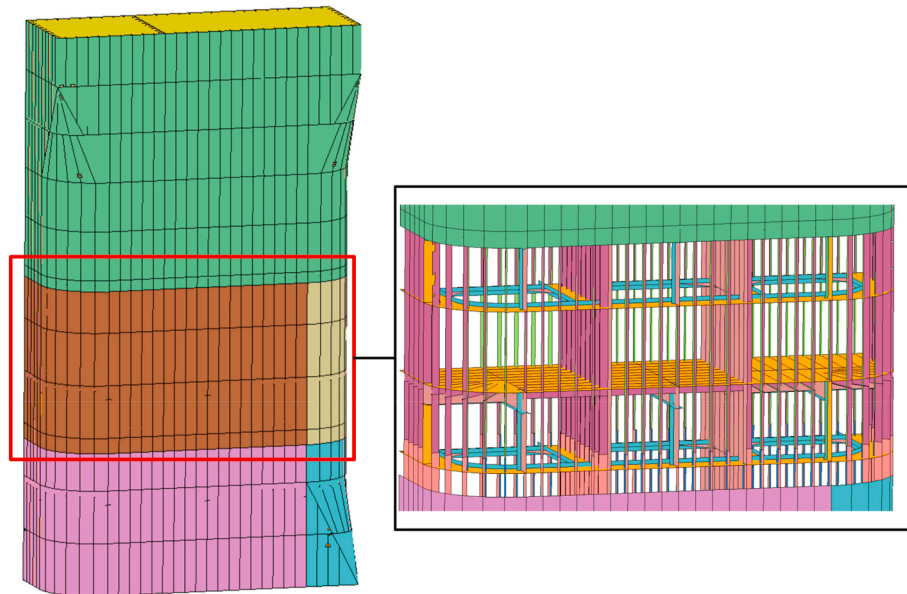
Fig. 13. The section of the column.

Fig. 14. The finite element model of the structure column.

3. Verification and calibration of the numerical solver

3.1. Description of the global and local ice geometries

Before any verification can be carried out, a careful selection of the global ice geometry and local ice sharpness is necessary. It is important to distinguish between local and global geometries of an ice feature. The global geometry is decisive with respect to the mass and inertia of the ice body and the demand for energy dissipation, while the local geometry is essential with respect to resistance of the ice subjected to deformation (crushing, extrusion, etc.) at the contact point (Amdahl, 2019). The global geometry of the ice is selected to be a cuboid with the same length

Table 3
Properties of the steel material.

Steel Grade	Young's Modulus (MPa)	Yield Strength (MPa)	Poisson Ratio	Power law K (MPa)	Power law n
column plates	2.07×105	420	0.3	860	0.16
column HPs	2.07×105	355	0.3	780	0.22

and width of 30 m and a height of 10 m as shown in Fig. 4. This yields a total ice displacement of 8100 tons. The selection is based on the finding by Lu et al. (2019) that the lower limit of the detection capability of marine radars under extreme wave conditions is an ice body with a waterline of about 30 m.

Yu et al. (2020) studied the effect of local ice sharpness on the collision response of a stiffened panel in a platform column, and found that a critical sharpness exists, which maximizes the structural damage for a given energy demand. Ice with blunter local geometries will deform the structure as if the ice is virtually rigid, but with less structural indentation compared to that caused by ice with the critical sharpness. Ice with sharper local geometries will be crushed substantially. We

select two different ellipsoidal local ice models as used in Yu et al. (2020), representing a blunt (radius of curvature 2.35 m) and a sharp (radius of curvature 0.68 m) geometry, respectively as shown in Fig. 4. The local ice bodies are modelled with detailed solid meshes and the constitutive ice material.

As collisions and deformations are assumed to occur only in the local ice region, different locations of the local ice relative to the global ice cube will yield different eccentricities of the collision loads with respect to the ice CoG. Two load eccentricities are assumed. In Case 1, the center of the local ice is placed close to the waterline with a direction vector of [15 m, 6 m, 3 m] relative to the global ice CoG (see Fig. 4), including both in-plane and out-of-plane eccentricities. Case 2 contains only in-plane eccentricities, where the center of the local ice is given by vector [15 m, 6 m, 0 m] (see Fig. 5). For each load case, two local ice models with different sharpness are employed.

Rigid beams are used to connect the center of gravity (CoG) of the ice block as a whole to the rear of the crushable local ice model. The beam properties are calibrated to represent correctly the total mass and inertia of the entire ice block with respect to the CoG. The 6DOF hydrodynamic forces and moments are applied as user-defined loads at the ice CoG. The contribution of local ice to the total mass and inertia of the global ice is considered small. Therefore, the ice blocks in both Case 1 and Case 2
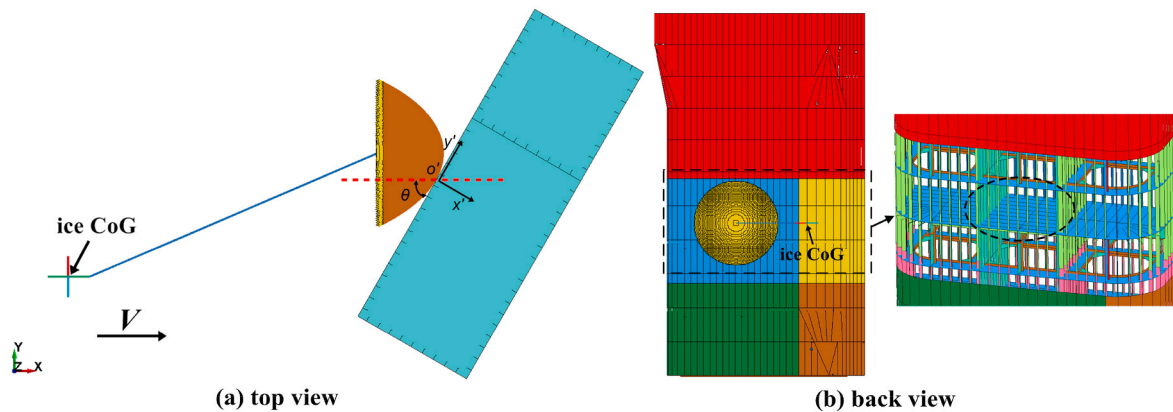

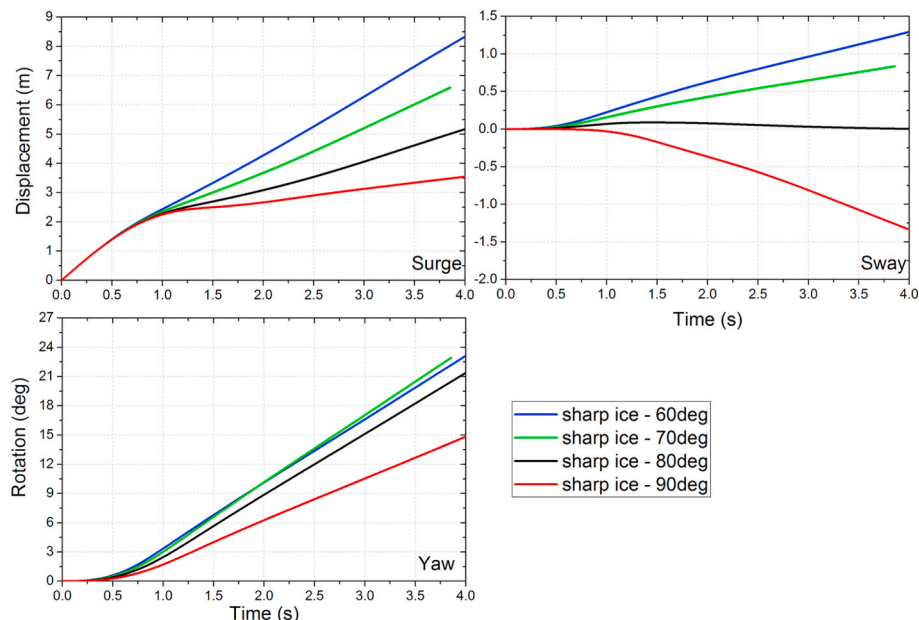**Fig. 15.** In-plane 3DOF glacial ice collision with a platform column.

Fig. 16. 3DOF motions at the ice block CoG with the sharp local geometry during and after collisions.
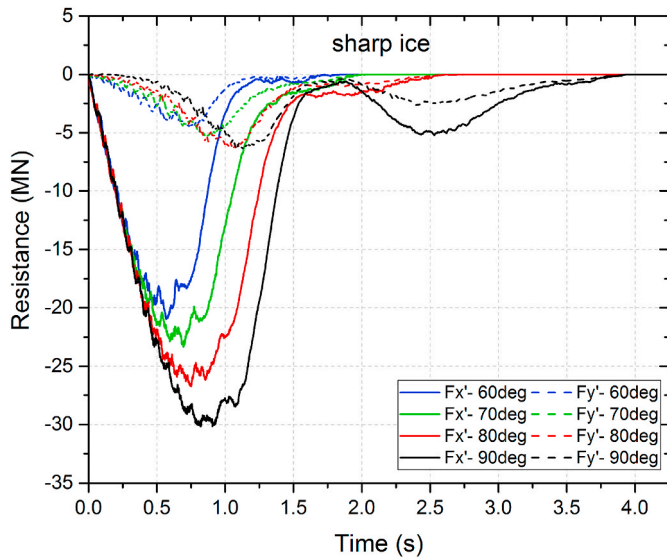
Fig. 17. The collision resistance during ice-platform collisions with the sharp local ice.

with either sharp or blunt local ice share the same global properties as shown in Table 2.

3.2. Verification of the implementation of hydrodynamic loads

In order to verify the implementation of hydrodynamic loads in LS-DYNA, numerical simulations were conducted with the ice configuration in Fig. 4 as an example (Case 1). The ice cube with a radius of curvature of 2.35 m (blunt) is given an initial velocity of 3 m/s and impacts a rigid plate; refer Fig. 6. The rigid plate is oriented with a normal vector of [-0.9254, 0.1632, -0.342] such that all 6DOF ice motions will be excited. Contact is considered only for the local ice body. The material parameters for the ice model and its calibration can be found in Section 3.3.

Fig. 7 shows snapshots of the ice cube motions during and after collisions with the initial ice state at t = 0.0 s as the reference configuration. The transparent part shows the current ice configuration at different time instants. The time histories of collision forces and moments are plotted in Fig. 8 with respect to the ice CoG. In the early stage, the local ellipsoidal ice is crushed substantially by the rigid plate. The ice cube moves initially in the negative heave direction under the action of negative vertical collision forces. The out-of-plane loading eccentricity induces significant pitch motions, while large yaw motions are observed due to in-plane loading eccentricity.

In order to verify the implementation of hydrodynamic loads in LS-DYNA, a user code was developed to solve numerically the motion equation in eq. (1). The code uses the same information of mass, moments of inertial and hydrodynamic coefficients as used in LS-DYNA. The collision forces and moments with reference to the ice CoG calculated in LS-DYNA are used as inputs. The Euler method with midpoint integration is employed, which yields second-order accuracy for the position. The adopted timestep is 10^{-3} s and is considered sufficiently small.

The time-displacement curves for the 6DOF ice motions calculated using LS-DYNA and the user code are compared in Fig. 9. Good agreement is obtained in general, but with small differences in the amplitudes of the roll and pitch motions. However, the periods of both motions agree well. The implementation of the hydrodynamic loads is thus considered successful; the model is shown to be very versatile for simulation of complicated collision scenarios with reasonable accuracy.

3.3. Verification and calibration of the ice material model

The code for the ice material model was used consistently by Liu et al. (2011) and Yu et al. (2020). The implementation has been verified in a single element test, where nodes on one end of the solid element is fixed against all degrees of freedom and nodes on the opposite plane are forced to move in a displacement-controlled manner. The resulting evolution of the yield stress with the hydrostatic pressure agrees well with the theoretical curve.

In ALS ice collisions, the behavior of ice and structures are sensitive
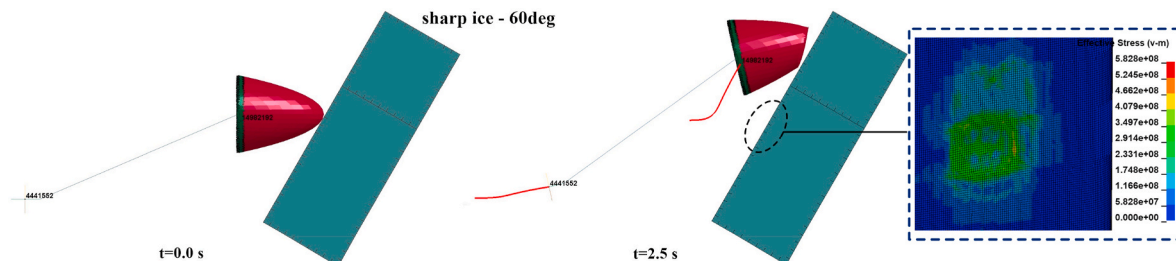

Fig. 18. Ice motion trajectories and structural damage during and after collision when the ice block with the sharp local geometry collides with the platform column with an angle of 60°.

Fig. 19. Ice motion trajectories and structural damage during and after collision when the ice block with the sharp local geometry collides with the platform column with an angle of 90°.
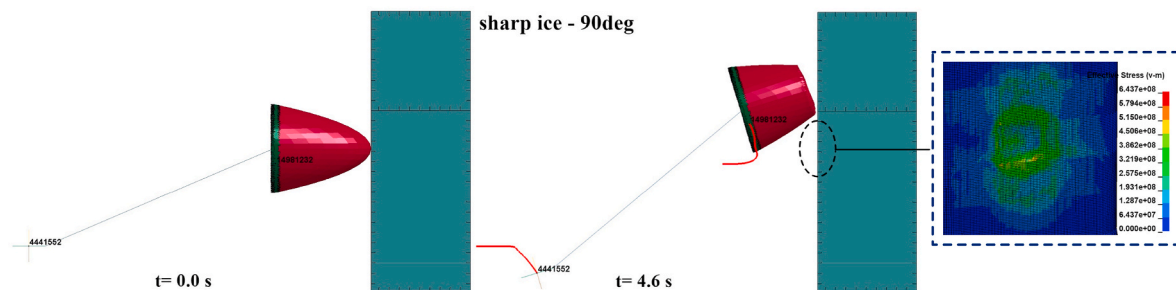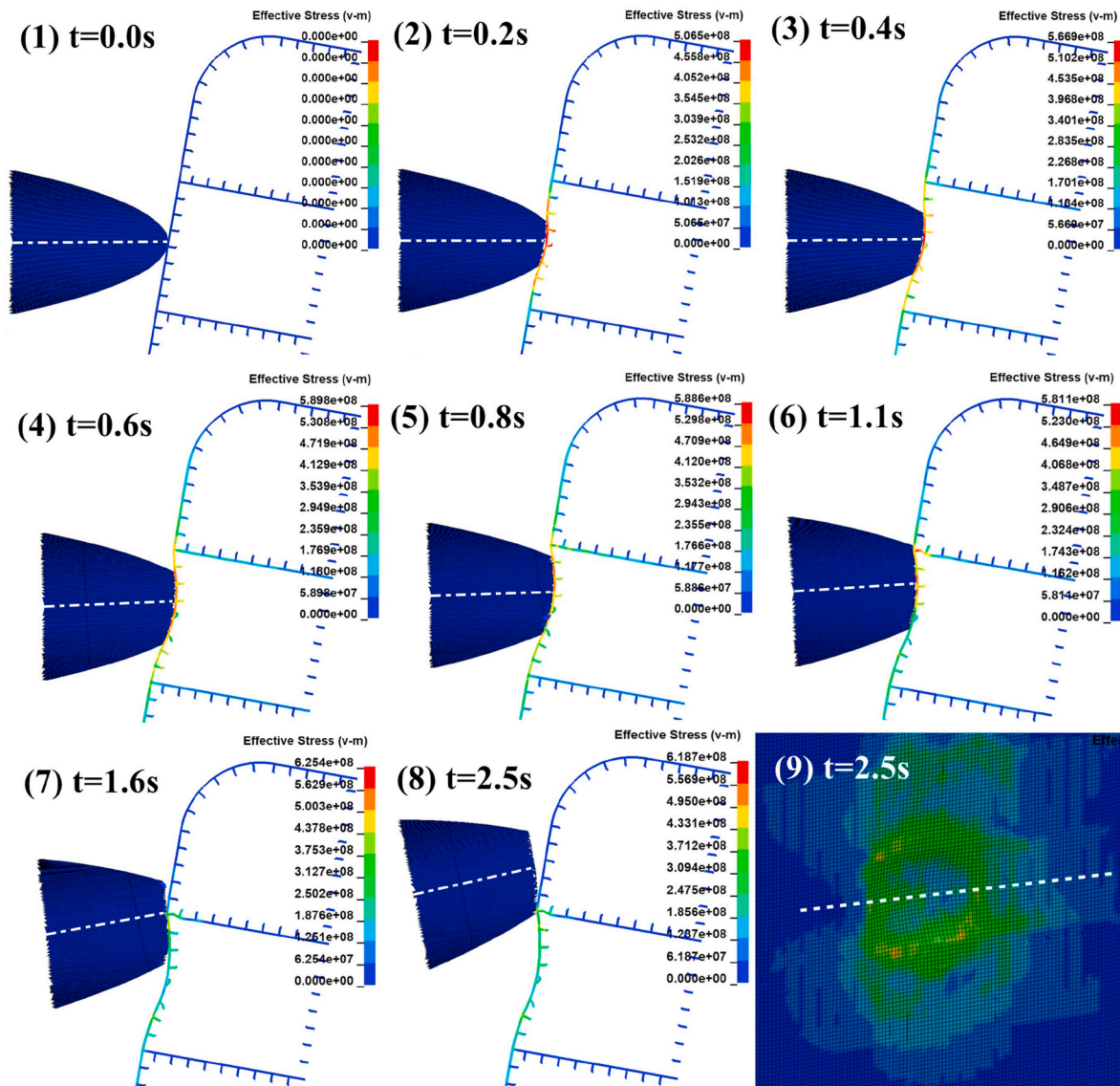
Fig. 20. Combined indentation and sliding damage during ice collisions for the case 'sharp ice – 80°'. The white dashed lines represent the center line of the ice.

to their relative strength. It is therefore crucial to calibrate correctly the energy absorption capability of ice in order to obtain a realistic structural response. A series of medium-scale indentation tests that were conducted in 1984, were employed to calibrate the ice material model. The tests (Kennedy, 1990) were conducted using a spherical indenter with a radius of 2.3 m driven by 4 hydraulic actuators; each hydraulic actuator had a capacity of 4 MN. The indented ice face was located in a lateral tunnel excavated into the side of a grounded iceberg, near the settlement of Pond Inlet on the northern coast of Baffin Island, NWT (Daley, 1994). Fig. 10 shows a sketch of the test arrangement.

Fig. 11 (a) shows plots of the force-displacement curves of 4 different cases from the Pond Inlet tests, with a common indenter radius of 2.3 m. The ice force indentation curves exhibit significant scatter, which demonstrates the inherent uncertainties of ice mechanical properties and responses. An analysis of the experimental data is carried out by averaging the ice energy absorption per unit crushed volume, which yields an ice crushing energy density of approximately 3 MJ/m^3 (Lu et al., 2018). This energy density correlates with a pressure area relationship of $p = 3.2A^{-0.1}$ (MPa), which is the local ice-load for PC3 vessels in the IACS polar class code (IACS, 2011). PC3 represents the vessel capability in the year-round operation in second-year sea ice, which may include multiyear ice inclusions. It differs greatly from the design

pressure curve for ULS actions. For ULS design, the ISO 19906 standard (ISO-19906, 2010) recommends an ice pressure area relationship of $p = 7.4A^{-0.7}$ (MPa) when $A \leq 10 \, m^2$ / $p = 1.48$ (MPa) when $A > 10 \, m^2$ for designing structures against local ice loading. A comparison of the IACS PC3 curve and the ISO curve for the ice pressure is given in Fig. 11 (b). The ISO curve gives a very large pressure for small contact areas, but the pressure decreases rapidly when the contact area increases. The local pressure is smaller than the ISO pressure-area curves for $A < 4 \, m^2$ and larger for $A > 4 \, m^2$. The ISO curve was derived from a series of indentation tests in the Beaufort Sea, including the Pond Inlet tests, and the values were determined by the mean value plus three times the standard deviation. This yields an approximate upper envelope of ice strength. The corresponding ice energy density is much larger than the average value from the tests, especially when the contact area is small; refer Fig. 11 (a). In ALS conditions, large deformations are expected either in ice or the structure or both, and thus, require a more realistic representation of ice energy absorption capability. The IACS PC3 pressure-area relationship of $p = 3.2A^{-0.1}$ (MPa) fits well the average ice energy absorption of the Pond Inlet experimental data and is adopted for further analysis.

The ice model employs a strain-based fracture criterion in Eq. (4), which renders the model sensitive to the adopted mesh size.
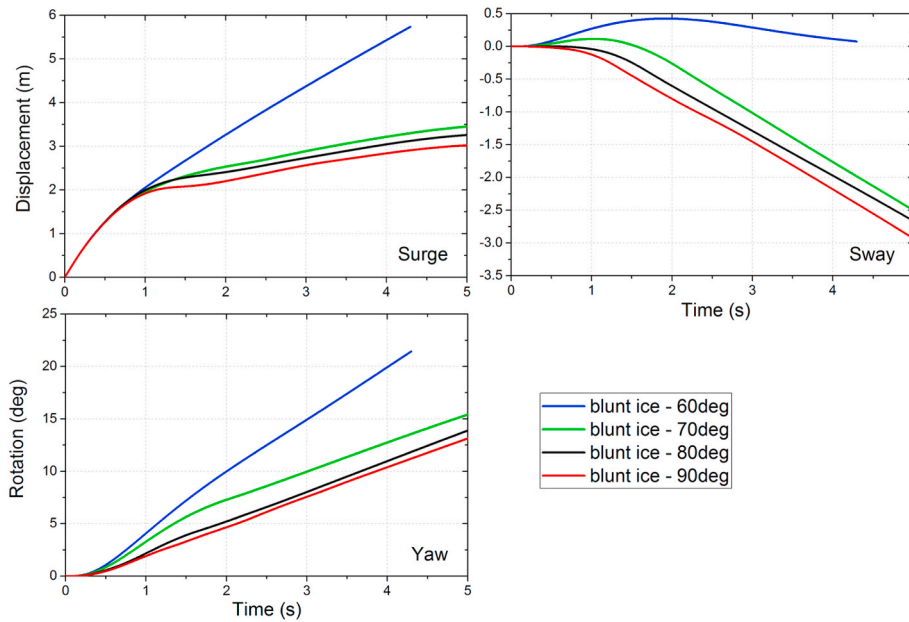
Fig. 21. 3DOF motions of the ice block with the blunt local ice during and after collisions.
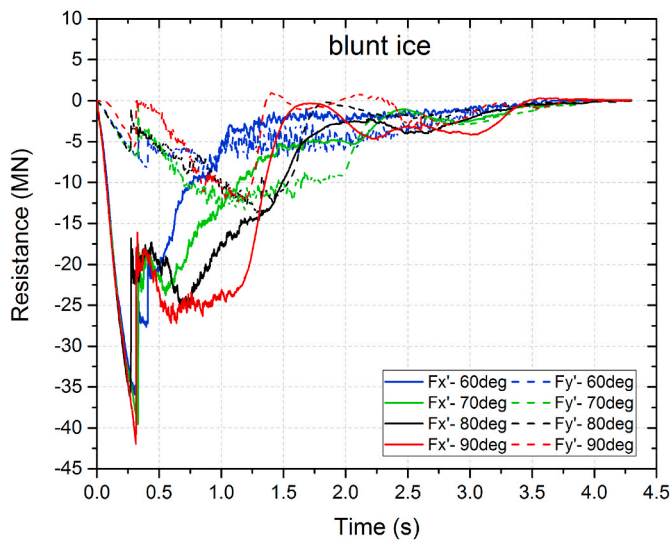

Fig. 22. The collision resistance during ice-platform collisions with the blunt local ice.

Furthermore, as modelling of the target ellipsoidal shapes with the same mesh size is difficult, calibration of the ice failure criterion has to be performed on a case-by-case basis. The two ellipsoidal ice models with different sharpnesses are meshed with solid elements with a size ranging from 35 to 75 mm. The two models are calibrated to the target ice design curve of $F = 3.2A^{0.9}$ (MN) in Fig. 12 by crushing with rigid plates as done in Yu et al. (2020). The calibrated force curves follow the design ice resistance curve well with small oscillations. The calibrated ice failure strain tends to decrease as the ice geometry becomes sharper.

3.4. Validation of the BWH fracture criterion

The code for the BWH (Bressan-Williams-Hill) instability criterion was initially proposed and implemented by Alsos et al. (2008) and has been validated of good accuracy by comparison of various collision experiments in Alsos et al. (2008) and Storheim et al. (2015).

4. Application of the proposed solver to glacial ice impacts on a semi-submersible platform column

The proposed solver can be used to simulate various glacial ice impact problems considering hydrodynamic-ice-structure interactions. An example is given below for ice collision on a semi-submersible platform column.
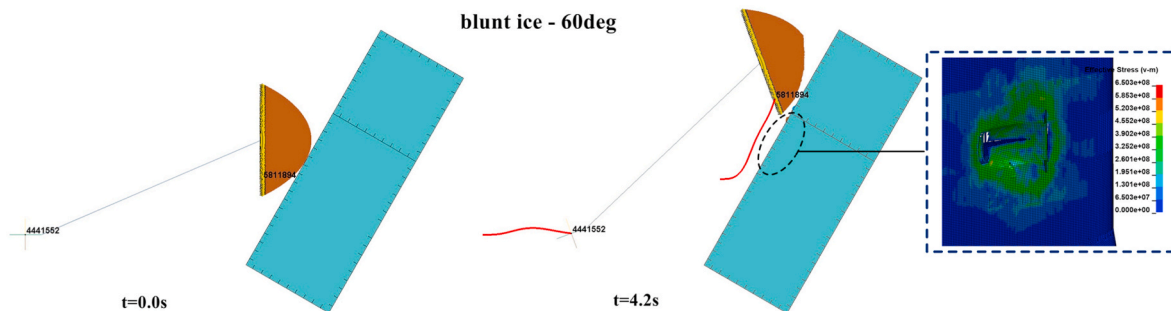

Fig. 23. Ice motion trajectories and structural damage during and after collision when the ice block with the blunt local geometry collides with the platform column with an angle of 60°.

Fig. 24. Ice motion trajectories and structural damage during and after collision when the ice block with the blunt local geometry collides with the platform column with an angle of 90°.
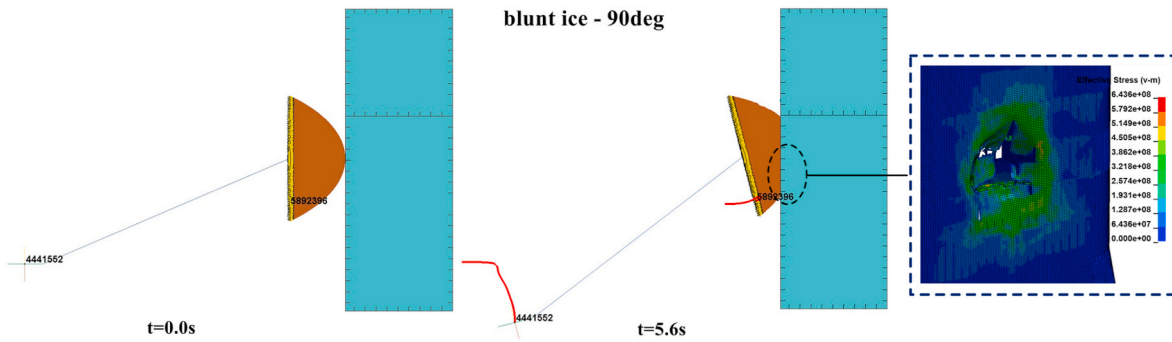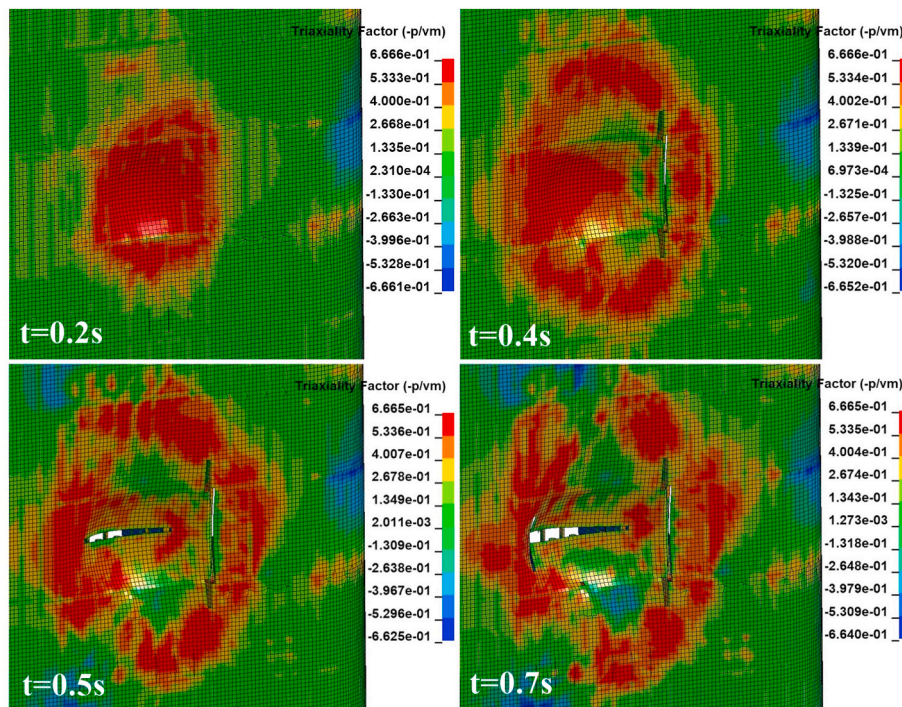

Fig. 25. Fracture initiation and propagation of structures during ice sliding for the case 'blunt ice – θ = 60°'. The contour plots represent stress triaxialities of elements.

4.1. Finite element models of the platform column

The column leg of the Midgard structure was modelled by Tavakoli and Amdahl (2010) for the assessment of structural strength against supply vessel collisions. The drawings of the platform column are shown in Fig. 13. The column was modelled from EL8125 through EL39000 in Fig. 13. Only the front part of one leg was modelled. The overall dimension of the FE-model shown in Fig. 14 is 17200 mm × 30875 mm x 6100 mm (w x h x d).

The outer shell thickness is in the range of 16–18 mm. The vertical stiffeners are equally spaced with a distance of 0.625 m. The stiffeners are modelled as L-bars with dimensions of 320x50x12x40 (mm), 300x50x11x50 (mm) and 240x40x10x30 (mm) depending on the locations. The column decks and the vertical bulkheads are equipped with stiffeners every 0.625 m. The thickness of the deck shell plating is 12 mm and 14 mm for the bulkhead plating. The column model was meshed using approximately 245,000 shell elements. The general element size is 120 mm.

Two steel material grades are used for the structure. The material properties and power law parameters are listed in Table 3. The column

plates have a yield stress of 420 MPa, while the column stiffeners are fabricated with a yield stress of 355 MPa. The BWH fracture criterion and element erosion are described in Section 2.3.

4.2. In-plane 3DOF coupled simulation of ice-platform collisions

First, in-plane 3DOF (Case 2) ice collisions on the platform column are studied with the ice configuration given in Fig. 5. The two calibrated local ice models with an initial curvature radius of 0.68 m and 2.35 m were adopted representing sharp and blunt local ice body, respectively. The collision scenarios are defined in Fig. 15, where the ice body hits the panel with an initial surge velocity V = 3 m/s. The mass and inertia of the semi-submersible platform are considerably larger than the studied ice such that any motion of the platform is neglected. The nodes on the top, bottom and rear sides of the platform column are fixed against translations and rotations. The *eroded_single_surface* contact is used to define the internal contact of the ice model and the *eroded_surface_to_-surface* contact for the contact between ice and the structure using the pinball segment-based contact with *SOFT* = 2. An ice friction coefficient of 0.15 is used. The collision angle as defined in Fig. 15 is θ = 60°, 70°,
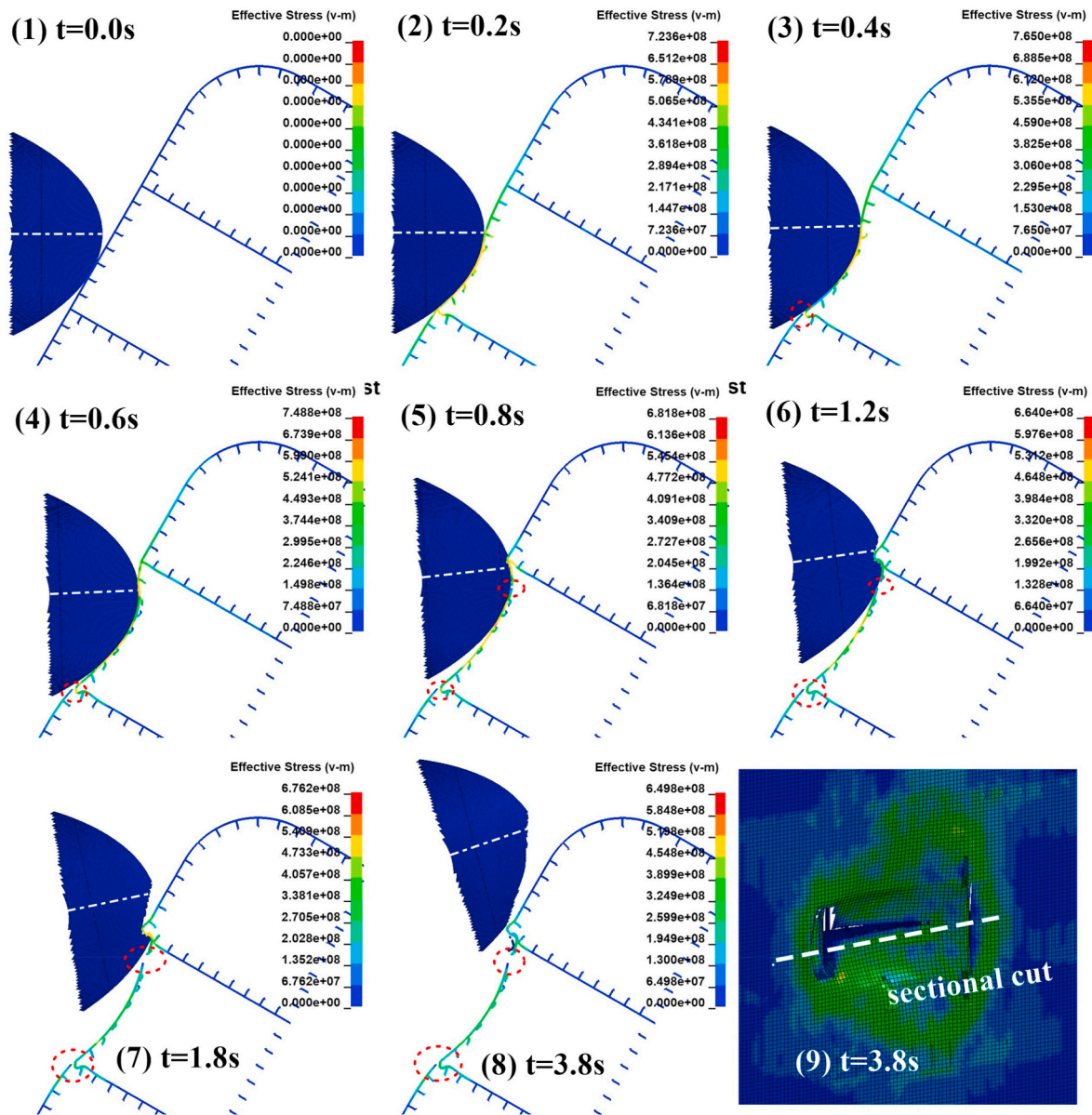
Fig. 26. Combined indentation and sliding damage during ice collisions for the case 'blunt ice – θ = 60°'. The white dashed lines represent the center line of the ice.

80° and 90°, respectively.

4.2.1. Ice motions and structural damage

- Ice collisions with sharp local ice

For ice-platform collisions with the sharp local ice, Fig. 16 displays time history of the 3DOF planar motions of the ice block during and after collision for different collision angles, and Fig. 17 plots the corresponding collision resistance in the local $x'o'y'$ coordinate as shown in Fig. 15. The collision angles in the studied cases are quite large. However, due to the small ice friction ($\mu_0 = 0.15$) and the load eccentricity, ice blocks can still slide to different extents and detach from the platform in the four cases. In general, a smaller collision angle yields larger yaw and sway motions. For cases with collision angles of 60° and 70°, the ice sway motions increase continuously with time. This is the typical *sliding* case as defined in external dynamics. An example of the sliding trajectory and structural damage is given in Fig. 18 for case 'sharp ice – θ = 60°', where the ice slides smoothly away from the platform.

For the case with a collision angle of 80°, the sway motion increases

initially, but starts to decrease after a while. For the case with a collision angle of 90°, the sway motion goes directly to a negative value. Fig. 19 illustrates the negative sway motion and ice trajectories for the case 'sharp ice – θ = 90°'. The reason for negative sway motions is that the deformed structure at the contact region tends to prevent the local ice from further sliding, and then the rotation center of the ice shifts from the ice CoG to the contact region. The ice turns out to rotate anti-clockwise about the contact region, and thus yields a negative sway. This is termed as *'the motion locking effect'*, and a direct result of this effect is the shift of rotation center from CoG to the contact region. This effect is also observed in ship collisions, e.g. Yu et al. (2016). In addition, due to the rebound effect, the ice still manages to detach from the platform.

From Figs. 18 and 19, the local sharp ice gets crushed significantly in both cases due to its relatively weak strength. The stiffened panel deforms but no rupture of the outer shell occurs. The collision resistance is governed by combined ice crushing and structural deformation. The deformation of either side increases the contact area and thus the resistance. The ice-structure interactions in ALS conditions are explained in detail in Yu et al. (2020).
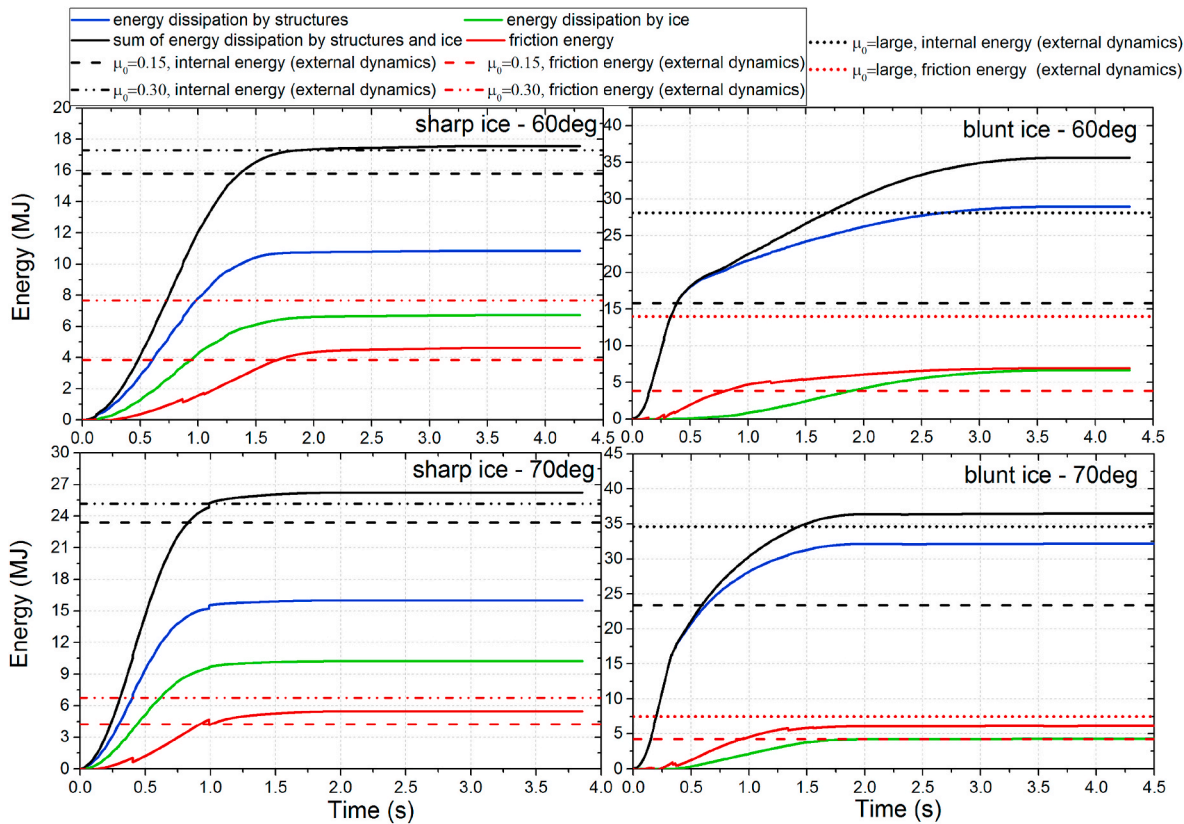
Fig. 27. Comparison of energy dissipation from numerical simulation and that predicted by external dynamic model for the case 'sharp ice – $\theta = 60°$', 'blunt ice – $\theta = 60°$', 'sharp ice – $\theta = 70°$' and 'blunt ice – $\theta = 70°$'

When hydrodynamic loads are introduced successfully, realistic ice motions during collision enable simulations of the combined ice indentation and sliding damage simultaneously. Fig. 20 presents sectional views of ice crushing and structural damage under combined indentation and sliding action at different time instants for the case 'sharp ice – $\theta = 80°$'. In the first 0.5s, the ice collides into the structure virtually straight with little lateral motions. During this period, both the ice and the structure deform, and the ice continuously decelerates in surge and accelerates in sway and yaw. From 0.6s, the sliding motion becomes evident and the ice moves continuously along the panel over time. Stiffeners along the sliding path deform slightly without tripping. The ice slides away from the platform after 2.5s with little damage imposed on the bulkhead. In general, the combined indentation and sliding loads tend to extend structural damage to a broader region compared to cases with indentation only. However, because of the relatively low strength of the sharp local ice, the damage extension is moderate in this case.

- Ice collisions with blunt local ice

For the blunt local ice collision with the platform, Fig. 21 displays time histories of the 3DOF planar motions of the ice block during and after collision for different collision angles. Fig. 22 plots the corresponding collision resistance in the local $x'o'y'$ coordinate. The ice motion trajectories and structural damage before and after collisions are shown in Figs. 23 and 24 for two representative cases i.e. 'blunt ice – $\theta = 60°$' and 'blunt ice – $\theta = 90°$'. From Fig. 22, the collision resistance is dominated by damage of the structure and the force curves in the x' direction virtually overlap with each other in the first quarter second.

For the case with a collision angle of $60°$, ice sliding is dominant, but *the motion locking effect* also exists with a negative sway velocity after 2s due to the presence of the bulkhead as shown in Fig. 21. The bulkhead

represents strong points of the structures and is capable of crushing the blunt ice significantly. It tends to prevent the ice from further sliding with a strong negative force in sway, but the ice manages to detach from the platform with significant kinetic energy as shown in Fig. 23. Sliding of the blunt ice causes severe damage and fracture of the structure. Fig. 25 shows fracture initiation and propagation as well as contour plots of element stress triaxialities during ice sliding. Triaxialities in the range of 0.66 indicate significant biaxial stretching. Once an initial crack occurs, stress concentration at the crack tip will cause continuous tearing of the panel.

For cases with collision angles of $70°$, $80°$ and $90°$, *the motion locking effect* becomes significant. The strong ice penetrates into the stiffened panel with large structural damage as shown in Fig. 24. The ice motion is locked by the deformed structure and the strong bulkhead. The contact bodies are not able to separate via ice sliding. The rotation center of the ice then shifts from CoG to the contact region. This yields a large negative sway motion and an anti-clockwise yaw motion about the contact region. However, due to the rebound effect and the yaw motion, the striking ice can still detach from the platform in the end.

Fig. 26 presents sectional views of ice crushing and structural damage at different time instants for the case 'blunt ice – $\theta = 60°$'. In the initial half second, the ice collides into the structure in virtually straight line with little lateral motions, but the initial inclination introduces loads in the tangential direction. The ice remains virtually undamaged during this period while the stiffened panel deforms significantly with large indentation and tripping of stiffeners. From 0.6 s, the sliding motion becomes evident and the ice slides continuously along the panel, causing large deformation and tripping of stiffeners along its path. The ice deformation is small until it hits the bulkhead of the column and starts to be crushed significantly. The curves in Fig. 22 show that the collision resistance drops drastically at about 0.3 s due to outer shell rupture and remains small during sliding. Because of the large kinetic
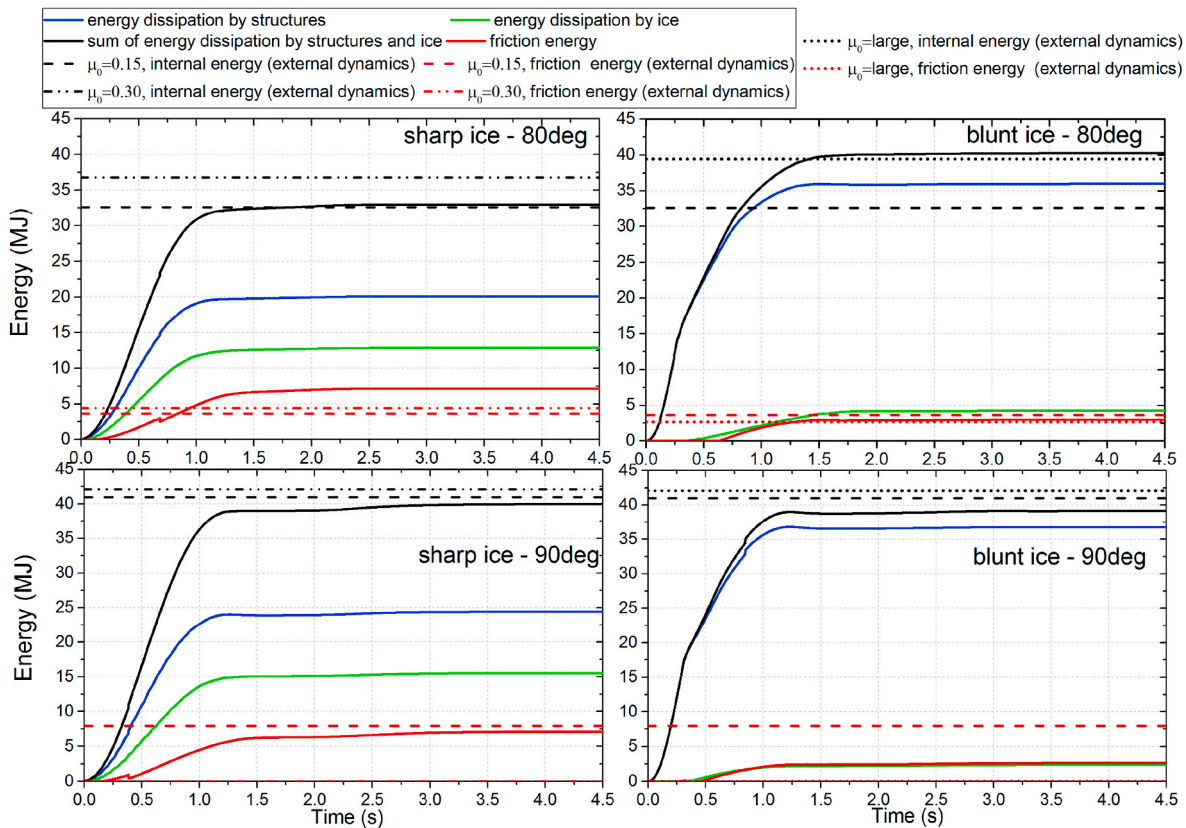
Fig. 28. Comparison of energy dissipation from numerical simulation and that predicted by external dynamic model for the case 'sharp ice – θ = 80°', 'blunt ice – θ = 80°', 'sharp ice – θ = 90°' and 'blunt ice – θ = 90°.
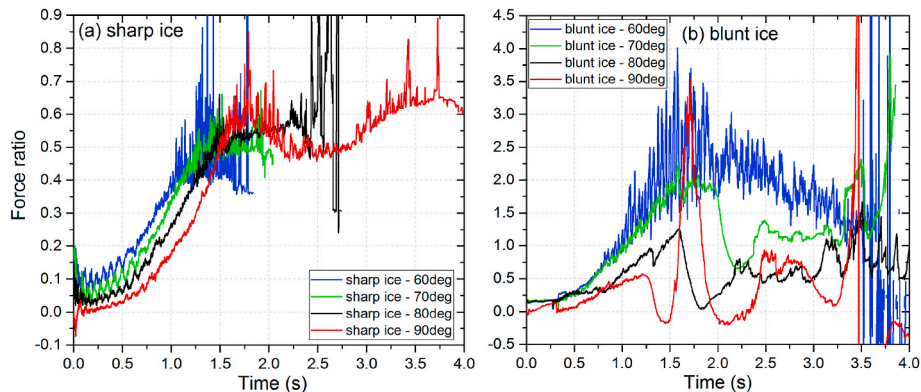

Fig. 29. The ratio of forces in the tangential and normal direction for collisions with the sharp ice model.

energy, the ice slides away from the platform at about 3.8s with a significant part of the local ice body completely removed by the bulkhead. It is interesting to find from Fig. 26 (8) that some removed ice pieces are left in the corner close to the bulkhead.

The results indicate that with strong ice, the combined indentation and sliding loads can cause significant extension of structural damage at a much smaller force level than for lateral indentation. This may induce progressive damage of the structure and significant degradation of the residual strength. In addition, the combined indentation and sliding loads may also speed up propagation of cracks and cause rupture in a wide area.

4.2.2. Energy dissipation

External dynamic models based on rigid body dynamics are often used for rapid prediction of the dissipated energy in a collision. Figs. 27 and 28 compare the dissipated energy calculated from the coupled simulations and that predicted by the external dynamics model by Liu and Amdahl (2010) for collisions from blunt and sharp ice with different collision angles. For the external dynamics model, the infinite frequency added masses of the ice body calculated by the boundary element method in the HydroD software are used. A restitution factor of 0.0 is adopted to be conservative.

In the external dynamic models, the status of the striking and struck objects after collision can be classified into two categories, i.e. *'sliding'* and *'sticking'*. It is governed by the ratio of the impact impulse $\mu = I_t/I_n$ relative to the friction coefficient μ_0, where I_t and I_n are the impact impulses in the tangential and normal directions, respectively. Collisions are categorized as *'sliding'* when $\mu \geq \mu_0$, and are *'sticking'* otherwise.
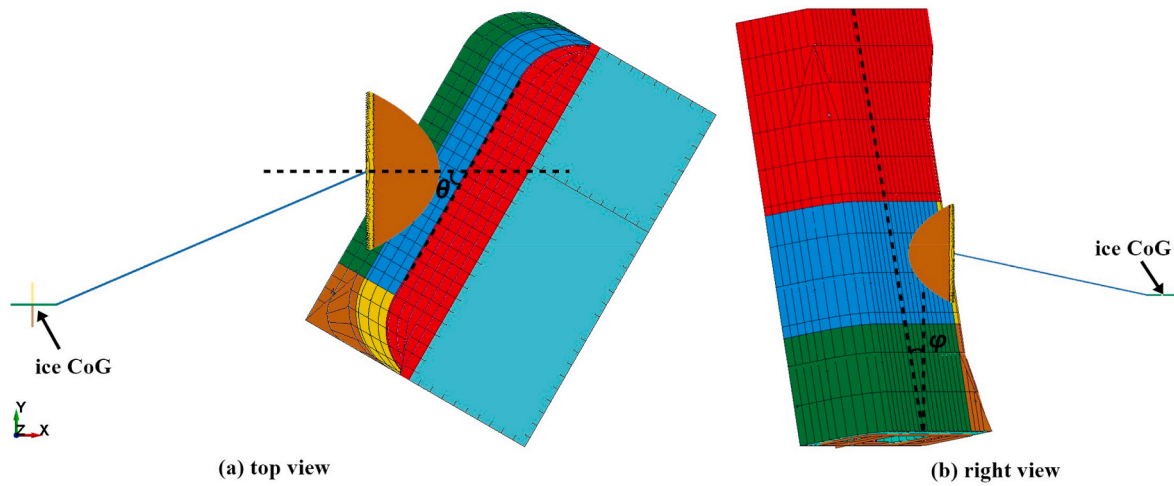
(a) top view

(b) right view

Fig. 30. FE model for 6DOF simulation of glacial ice collision with a platform column.
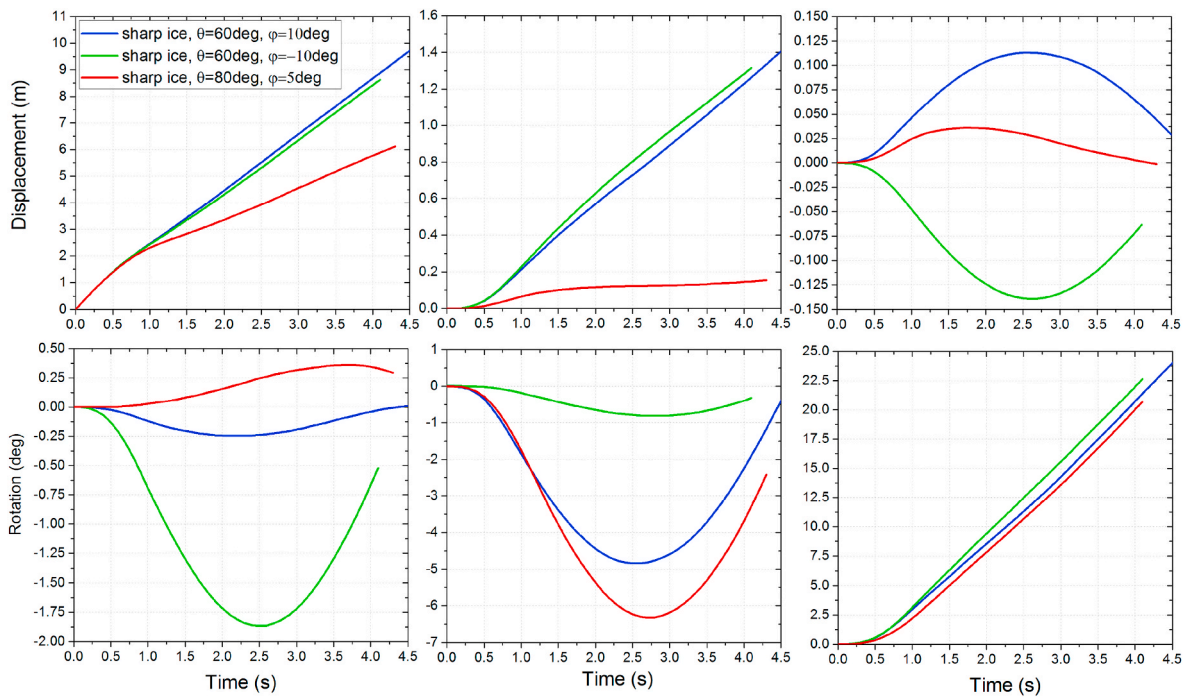

Fig. 31. 6DOF motions of the ice block with the sharp local ice during and after collisions.

Because of a small ice friction coefficient of $\mu_0 = 0.15$ and the load eccentricities, the external dynamic model predicts all the above eight cases to be *'sliding'*. In addition, given the same collision angle and friction coefficient, the external dynamic models do not distinguish whether the striking ice is sharp or blunt, and predicts the same dissipated internal and friction energy.

From the coupled simulations, it is not quite straightforward to tell whether collision for a specific scenario belongs to *'sliding'* or *'sticking'*, and the prediction accuracy differs greatly for cases with sharp and blunt ice. For the cases with sharp local ice, the model by Liu and Amdahl (2010) predicts the dissipated energy with reasonably good accuracy in general. For collision angles of 60° and 70° with the sharp ice, the external dynamic model underestimates the internal energy to some extent. This may be due to underestimation of the tangential force by considering only friction but not the sliding forces. Liu and Amdahl (2019) proposed to use an equivalent friction coefficient by adding the columbic friction coefficient and the sliding force - indentation load

ratio. Fig. 29 plots the ratio of forces in the tangential and normal directions in Fig. 17 for both the sharp and blunt collision cases. From Fig. 29 (a) for sharp ice, the force ratio starts with the columbic coefficient of 0.15 and decreases in the initial 0.25 s because the deformation is governed by indentation with little sliding and friction forces. After that, the ratio increases continuously with increasing sliding motions up to a value of about 0.6 at 1.5s. By averaging the ratios over time, we may adopt an equivalent friction coefficient of 0.3. The results are shown in Figs. 27 and 28.

It seems that the predicted internal energy agrees better with the coupled simulation when $\mu_0 = 0.30$. Theoretically, an increase of the friction coefficient will lead to two conditions as follows:

- the ratio of the impact impulse μ remains larger than the new equivalent friction coefficient, i.e. $\mu \geq \mu_{0,eq}$, and the collision stays in the *'sliding'* regime. The internal energy increases continuously with increasing equivalent friction coefficients.
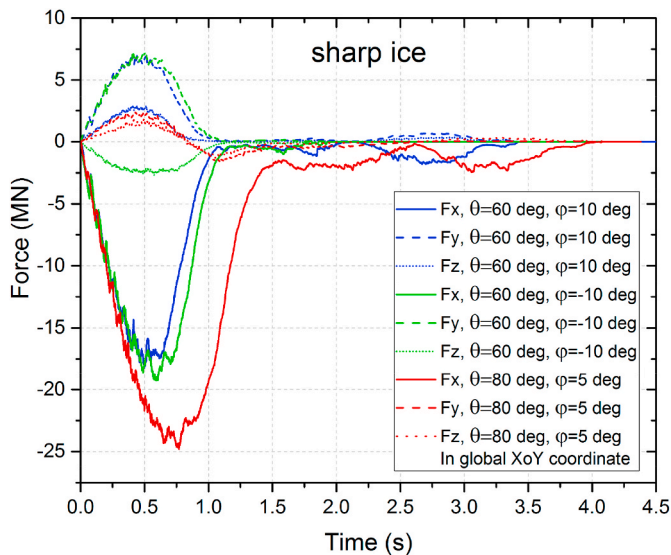
Fig. 32. The collision resistance with the sharp local ice in the global coordinate.

- the ratio of the impact impulse μ becomes smaller than the equivalent friction coefficient, i.e. $\mu < \mu_{0,eq}$, and the collision shifts to the *'sticking'* regime. The internal energy increases to a constant value and does not change with further increase of the equivalent friction coefficient.

For the collision cases with the blunt ice, the predicted internal energy shows large differences with the simulation results when only the columbic friction coefficient $\mu_0 = 0.15$ is used. The external dynamic model categorizes the four cases as *'sliding'* collisions. This does not hold in general for blunt ice collisions due to <u>the motion locking effect</u> with large structural damage and the presence of the strong bulkhead structure. Even for the case 'blunt ice – 60°' where the ice managed to slide away from the platform, the discrepancy is still significant. From Fig. 29 (b), the equivalent force ratio is considerably larger than the initial friction factor 0.15 due to the locking effect.

If we artificially increase the equivalent friction coefficient to a very large value, this will enforce a *'striking'* regime. According to the formulation of external dynamics, the collision energy in a *'striking'*

collision no longer depends on the frictional coefficient, but only on the collision angle. The predicted collision energy yields fairly good agreement for cases with collision angles of 70°, 80° and 90°. For the case 'blunt ice – 60°', the internal energy becomes better, but is still somewhat underestimated.

The authors have found that <u>the motion locking effect</u> widely exists in collisions, not only for ice collisions, but also for ship collisions, e.g. ship - offshore fish farm collision (Yu et al., 2019b), ship - jacket platform collision (Yu and Amdahl, 2018), ship - semi-submersible platform collision (Yu et al., 2019c) and ship - ship collisions. In cases where <u>the motion locking effect</u> is present, due to large structural deformation and possible rupture, the dissipated energy becomes larger than that predicted by external dynamic models. This is because external dynamic models assume collisions between rigid bodies, and do not consider cases with large structural deformations. In cases with significant motion locking effects, it is recommended to use a large equivalent friction coefficient as the input of external dynamic models to enforce a *'striking'* regime. This gives a better approximation of the dissipated internal energy with some conservation.

It becomes clear that determination of the friction coefficient for external dynamic models requires information of the relative strengths of the striking and struck objects, which is often not known a priori. Use of the columbic friction coefficient as input regardless of their relative strengths will yield unconservative results with respect to demand for strain dissipation.

4.3. 6DOF coupled simulation of ice-platform collisions

Both the column and the ice are often not in upright conditions due to their motions in waves. Therefore, in addition to the collision angle θ, a relative pitch angle ϕ is considered accounting for the relative pitch position of the colliding bodies at the instant of collisions, and the collision geometry shown in Fig. 30. The ice configuration Case 2 in Fig. 4 is used with both in-plane and out-of-plane eccentricities. The ice models with the two calibrated local ice are given an initial impact surge velocity V = 3 m/s. The nodes on the top, bottom and rear sides of the platform column are fixed against translations and rotations as in the 3DOF simulations. An ice friction coefficient of 0.15 is used. The ice collision angle is assumed to be $\theta = 60°$ and 80 while the relative pitch angles are $\phi = 5°$, 10° or −10°.

(a) sharp ice, θ=60 deg, ϕ=10 deg

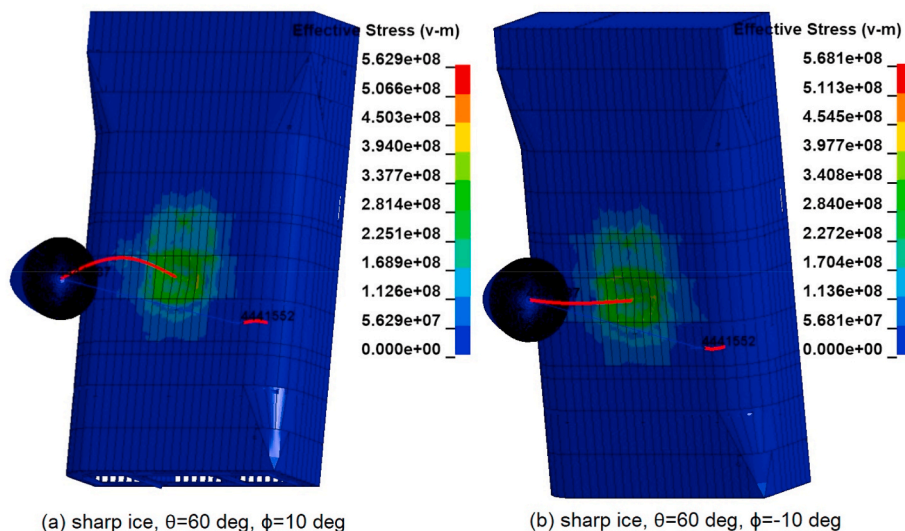

(b) sharp ice, θ=60 deg, ϕ=-10 deg

Fig. 33. Ice motion trajectories and structural damage during and after collision when the ice block with the sharp local ice collides with the platform column with θ = 60°, ϕ = 10° or −10°.

(a) sharp ice, θ=80 deg, φ=5 deg top view
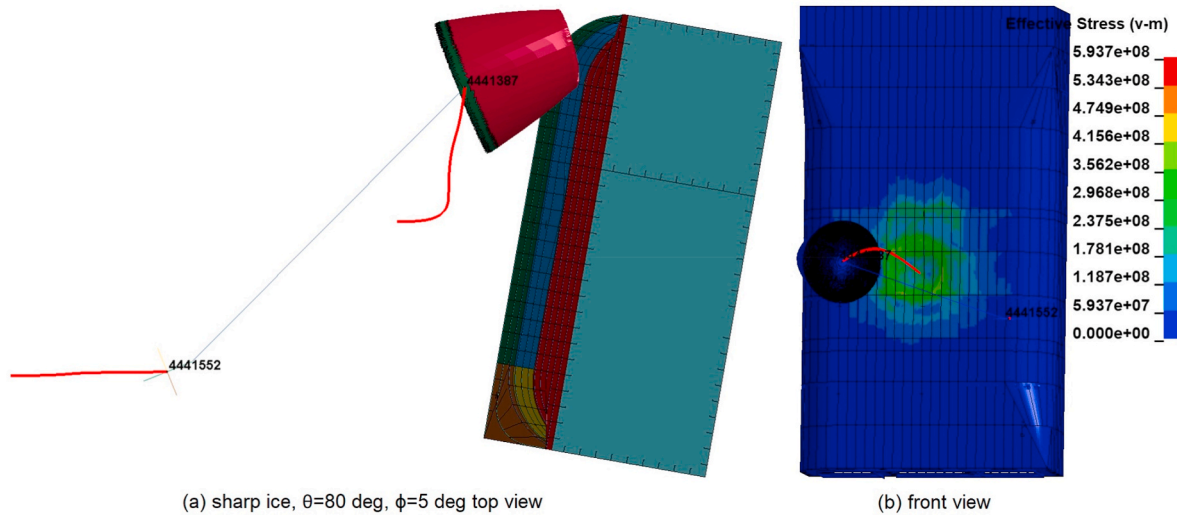
(b) front view

Fig. 34. Ice motion trajectories and structural damage during and after collision when the ice block with the sharp local ice collides with the platform column with θ = 80°, φ = 5°.
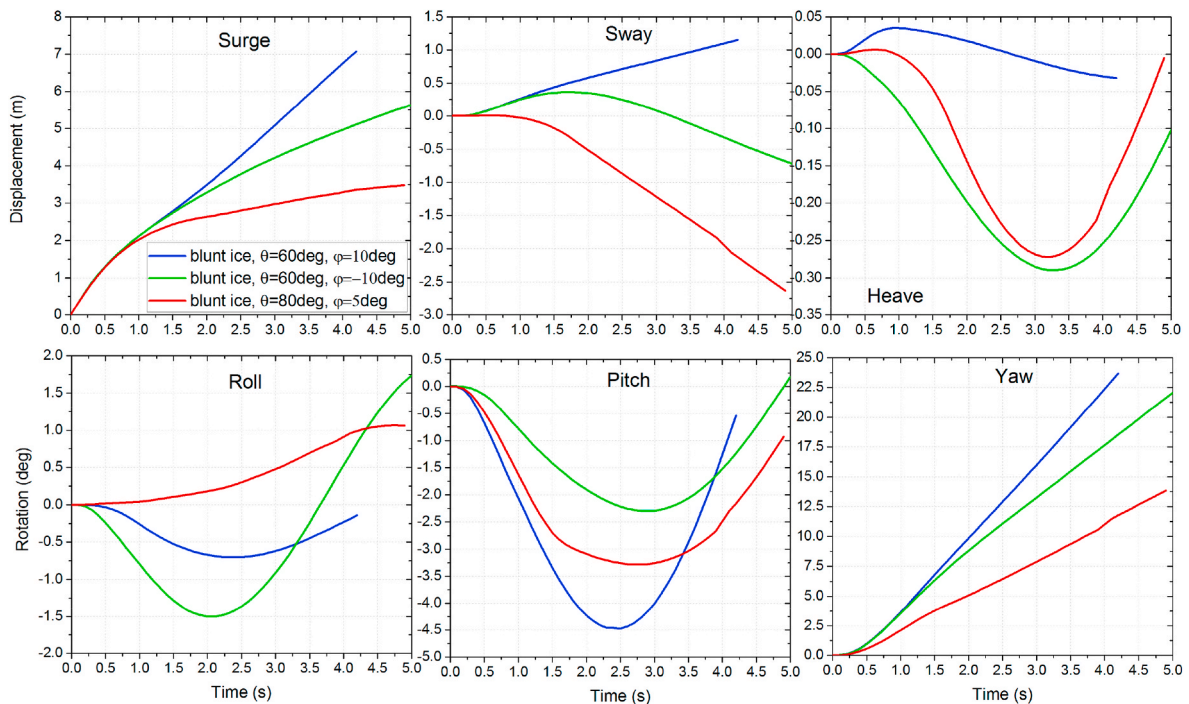

Fig. 35. 6DOF motions of the ice block with the blunt local ice during and after collisions.

4.3.1. Ice motions and structural damage

- Ice collisions with sharp local ice

For the 6DOF coupled ice-platform collisions with the sharp local ice, Fig. 31 plots the time histories of the 6DOF motions of the ice block during and after collision with different angles of θ and φ, and Fig. 32 plots the corresponding collision resistance in the global coordinate. Figs. 33 and 34 show the corresponding ice motion trajectories and structural damage during and after collision. The 6DOF ice motions are clearly observed. The pitch angle is significant for cases with φ = 5° or 10° because the heave (positive) and surge (negative) forces contribute jointly to a large negative pitch moment. For the case with φ = −10°, the contributions from forces in surge and heave cancel each other to some

extent, yielding a small pitch angle.

- Ice collisions with blunt local ice

For the three cases, the ice is capable of sliding away from the platform column. The local ice body is significantly crushed, while the stiffened panel is dented moderately without shell rupture. No decreasing sway motions with time are observed for the three cases. This indicates that with more degrees of freedoms activated, *the motion locking effect* becomes less significant.

For the 6DOF coupled ice-platform collisions with the blunt local ice, Fig. 35 plots the time histories of the ice block motion during and after collision for different values of the angles θ and φ. Fig. 36 plots the corresponding collision resistance in the global coordinate. Figs. 37 and
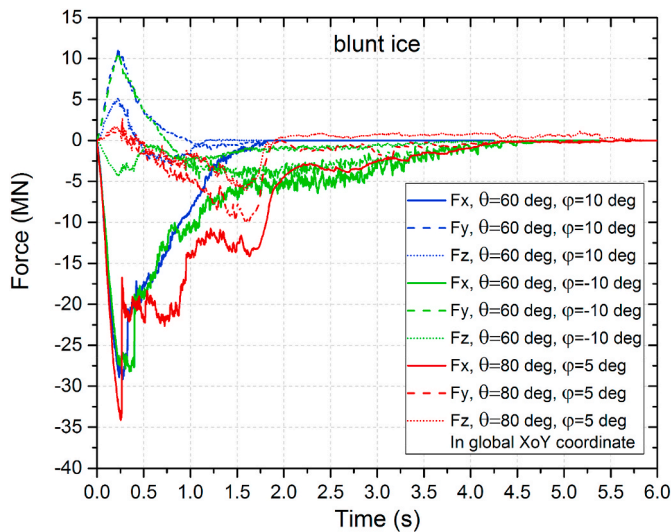
Fig. 36. The collision resistance with the blunt local ice in the global coordinate.

38 show the corresponding ice motion trajectories and structural damage during and after collision. The 6DOF ice motions are clearly observed and become quite complicated due to *the motion locking effect*.

For the case 'blunt ice - θ = 60°, φ = −10°', the pitch motion is moderate because contributions from heave and surge forces tend to counteract with each other. The ice manages to slide away from the platform with significant structural damage and rupture as shown in Fig. 37. The fracture pattern is quite similar to the corresponding 3DOF case. For the case 'blunt ice - θ = 60°, φ = 10°', the ice pitch motion is significant with joint contributions from heave and surge forces. The local ice slides upwards along the side panel, and this changes the fracture pattern. Fracture occurs at the panel boundaries as shown Fig. 37 due to large stretching rather than in the middle of the plate in the 3DOF case. This demonstrates the importance of considering 6DOF ice motions, as these may influence the failure pattern of the structure.

For the case 'blunt ice - θ = 80°, φ = 5°', the ice penetrates into the column panel with significant tearing of the structure. *The motion locking effect* is significant. Due to the large pitch motion, the cracks tend to propagate upwards, and the fracture patterns are not quite the same with that of the corresponding 3DOF case in Fig. 24.

4.3.2. Energy dissipation

Figs. 39 and 40 compare the dissipated energy calculated from the coupled simulations and that predicted by the external dynamic model by Liu and Amdahl (2010) for the studied 6DOF collisions from the blunt and sharp ice. The parameters that are adopted are identical to those in the 3DOF cases as concerns the infinite frequency added masses of the ice, the restitution factor of 0.0 and the columbic friction coefficient of 0.15. The external dynamic model predicts all the studied 6 cases to be '*sliding*'.

For the sharp ice cases, the predicted energy with $\mu_0 = 0.15$ shows a slight underestimation of the simulation results. The underestimation results from ignorance of sliding loads in the calculation of friction coefficient. An increased equivalent friction coefficient to 0.3 yields very good match of the simulated internal energy. It is noted that even for collisions from the sharp ice with weak strength, the structures absorb more energy than the ice itself.

For the blunt ice cases, *the motion locking effect* is significant. The predicted energy with $\mu_0 = 0.15$ underestimates significantly the energy from simulations. By using a large equivalent friction coefficient to enforce '*sticking*' conditions, we obtain good accuracy for the case 'blunt ice - θ = 80°, φ = 5°', and better agreement for the other two cases. The cases 'blunt ice - θ = 60°, φ = 10°' and 'blunt ice - θ = 60°, φ = −10°' with consecutive impacts from initially in panel middle panel to later at the bulkhead seem difficult to predict with the external dynamic models.

5. Discussions

The proposed solver has demonstrated good capabilities to simulate glacial ice impacts for ships and offshore structures accounting for the complex hydrodynamic-ice-structure interactions. It should be noted that the hydrodynamic loads are calculated based on the seakeeping linear potential flow theory without considering any viscous forces and hydrodynamic interactions between ice and the structure. Sayeed et al. (2017) reviewed the hydrodynamic interactions in the approaching process of iceberg and bergy bit towards offshore structures and emphasized the importance of near-field hydrodynamic interactions. Ommani et al. (2019) used linear potential flow theory to consider the multi-body hydrodynamics interactions when a glacial ice feature approached an offshore platform. The effect of viscosity was considered with Morrison type coefficients of drag forces. The current model may be extended to consider the effects of multi-body hydrodynamic interactions and the correction terms for viscous forces in future work.

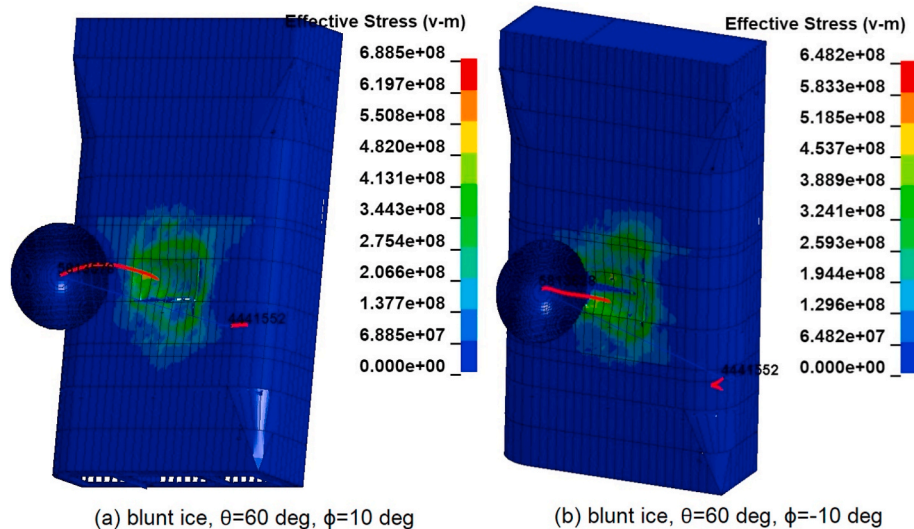Fig. 41 plots the evolution of total energy with time for all the studied

(a) blunt ice, θ=60 deg, φ=10 deg   (b) blunt ice, θ=60 deg, φ=-10 deg

Fig. 37. Ice motion trajectories and structural damage during and after collision when the ice block with the blunt local ice collides with the platform column with θ = 60°, φ = 10° or −10°.
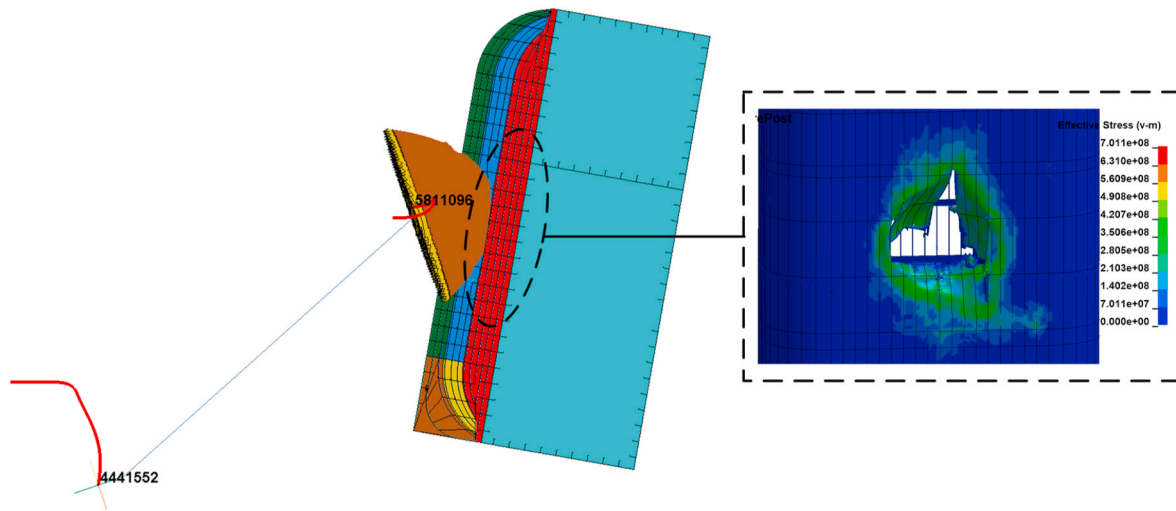
Fig. 38. Ice motion trajectories and structural damage during and after collision when the ice block with the blunt local ice collides with the platform column with θ = 80°, ϕ = 5°.
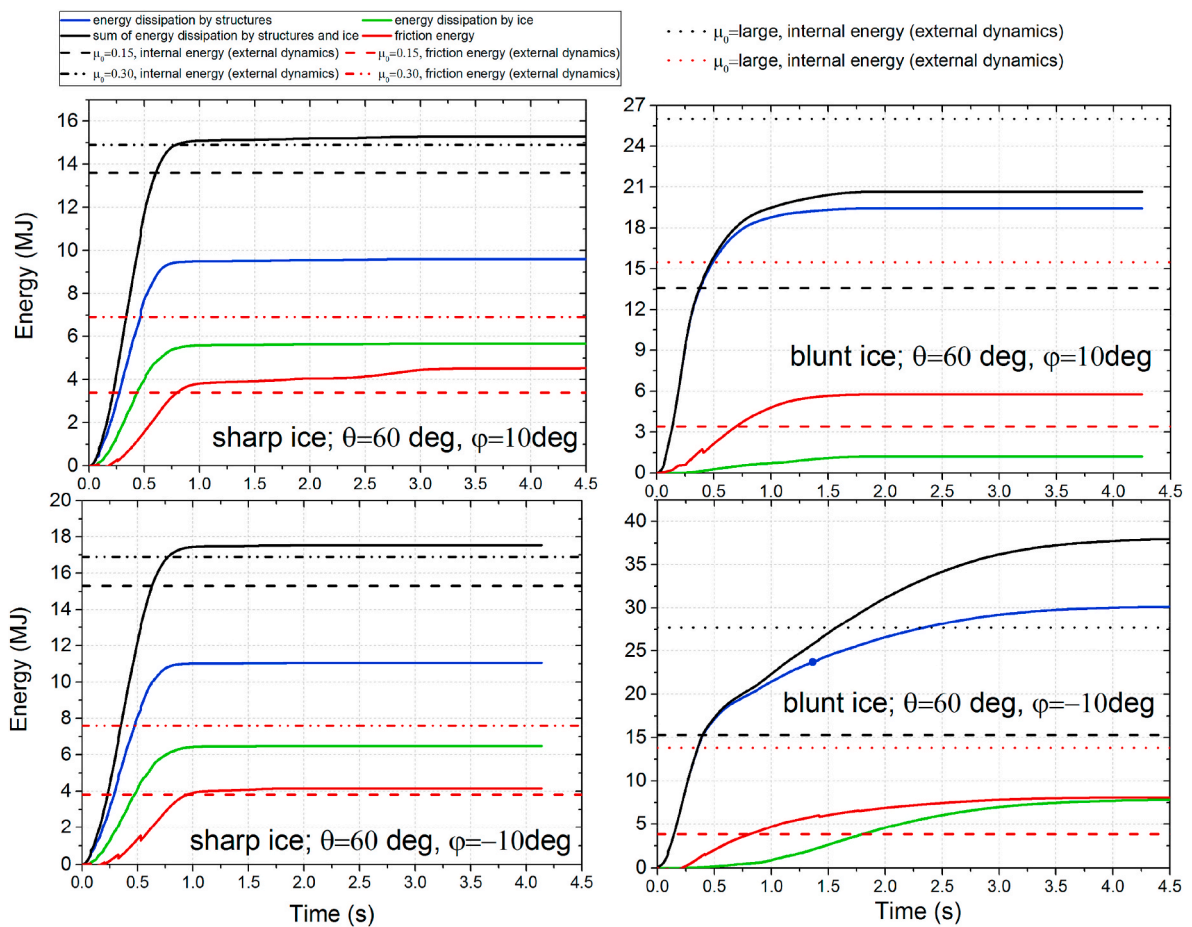

Fig. 39. Comparison of energy dissipation from numerical simulation and that predicted by external dynamic model for the case 'sharp ice - θ = 60°, ϕ = 10°', 'sharp ice - θ = 60°, ϕ = −10°', 'blunt ice - θ = 60°, ϕ = 10°' and 'blunt ice - θ = 60°, ϕ = −10°'.

3DOF and 6DOF collision cases. The total energy includes strain energy, friction energy and kinetic energy. Before collision, the ice block is in force equilibrium with a velocity of 3 m/s, and this gives a total energy of 36.45 MJ. When collision occurs, the actions from added mass forces in surge and the loads related to hydrodynamic memory effects increase the total energy in the system continuously. It is noticed that the energy

increases much faster for blunt ice impacts compared to sharp ice impacts because the magnitudes of accelerations for the blunt ice cases are considerably larger, which yields larger loads related to the added masses and the memory effects. In general, the total energy falls between the values considering infinite frequency and zero frequency added masses. This is consistent with observations by Petersen and Pedersen
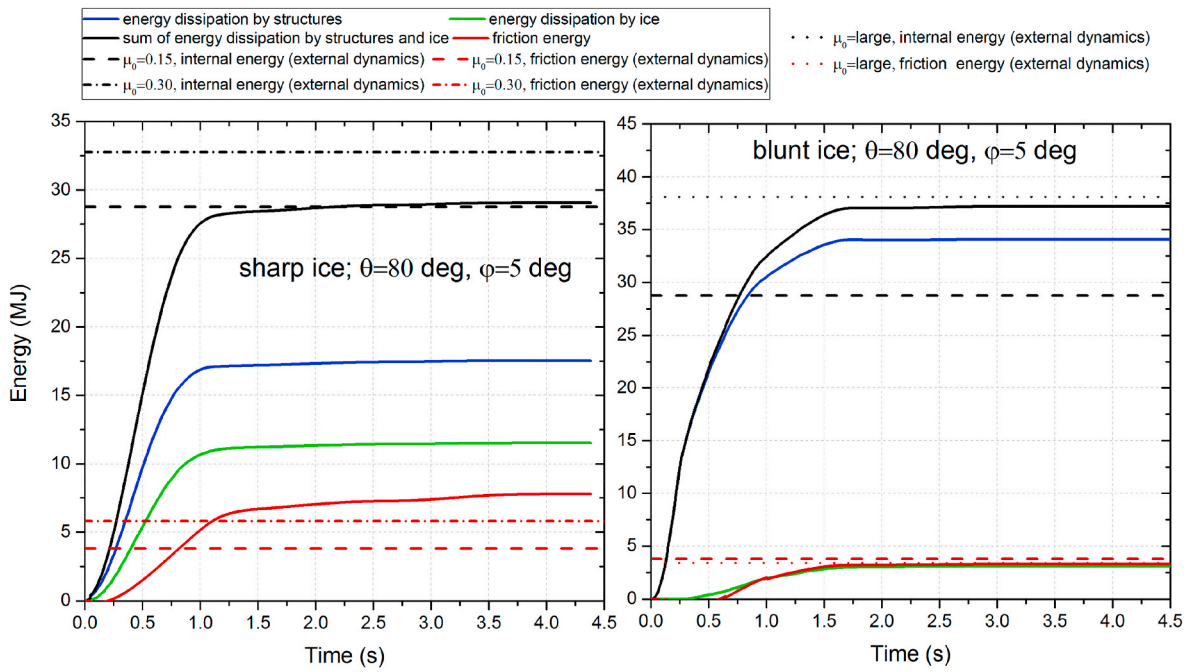
Fig. 40. Comparison of energy dissipation from numerical simulation and that predicted by external dynamic model for the case 'sharp ice - θ = 80°, φ = 5°' and 'blunt ice - θ = 80°, φ = 5°'
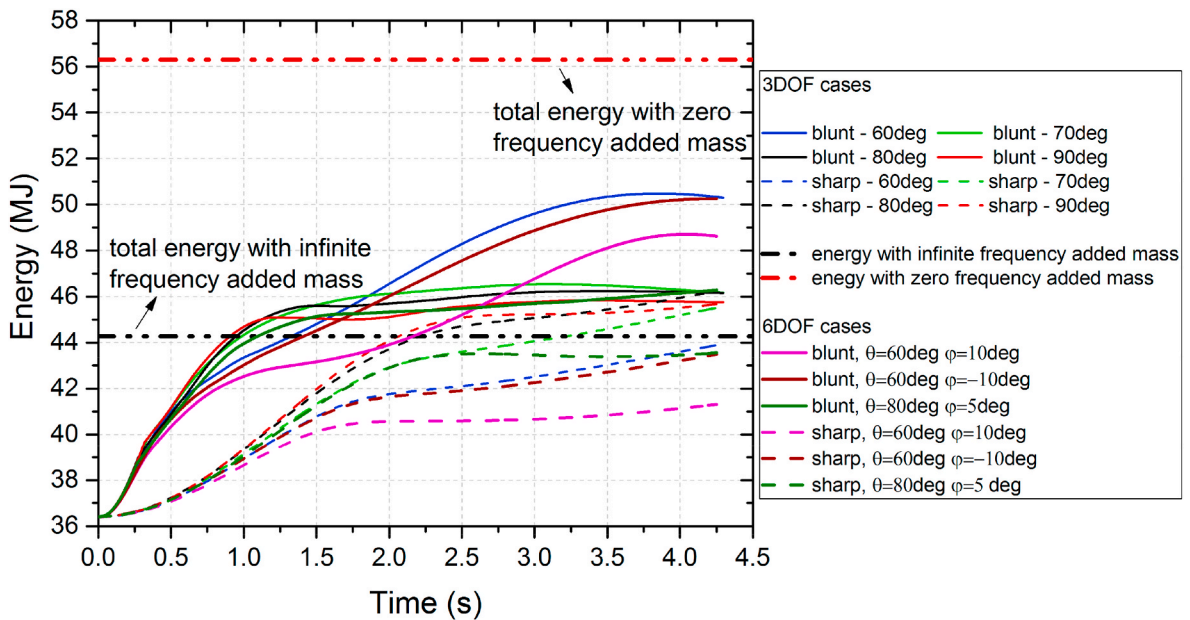

Fig. 41. Evolution of total energy with time for the eight cases.

(1981) and Motora et al. (1971), who discussed the equivalent added masses for ship collisions. Both papers dealt with the equivalent sway added mass for right angle collisions.

It is also noticed from Fig. 41 that for some cases in 6DOF collisions, the total energy can be smaller than the energy considering infinite frequency added mass. This is because the velocities in surge do not necessarily decreases to zero at the end of oblique impacts. The added mass contributions are therefore smaller than $1/2 m_{a,\inf} V^2$. In addition, for cases where the periodical motions heave, roll or pitch are significant, some energy is stored as potential energy related to the restoring forces, and this energy is not accounted for in the total energy in Fig. 41.

Based on the simulation results, it is recommended to use an equivalent added mass for practical estimation of the total energy with conservation, which equals an average of infinite frequency and zero frequency added masses, i.e.

$$E_{total} = \frac{1}{2}\left(m + m_{a,\,eq}\right)V^2$$

$$m_{a,\,eq} = \frac{1}{2}\left(m_{a,\,zero} + m_{a,\,\inf}\right)$$

(8)

6. Conclusions

This paper proposed a numerical solver for coupled dynamic simulation of glacial ice impacts. The solver utilizes the potential flow theory

for hydrodynamic loads, the BWH criterion for fracture prediction of metals and a constitutive ice material model. An example application of the solver is given for ice impacts on a semi-submersible platform column. The following conclusions are drawn:

1. The proposed solver has demonstrated high capabilities to simulate complicated scenarios of glacial ice impacts considering hydrodynamic-ice-structure interaction. The solver enables more realistic simulation of structural damage to ships and offshore structures under combined indentation and sliding ice loads. Its accuracy needs to be tested by comparing with experimental data in future work.

2. The combined indentation and sliding loads can cause significant extension of structural damage at a much smaller force level than for rectilinear indentation. This may induce progressive damage of the structure and significant degradation of the residual strengths after collisions. In addition, the combined indentation and sliding loads can also speed up crack propagation and cause rupture in a wide area. This effect is especially significant for collisions from blunt strong ice and should be carefully designed against.

3. For collisions from the sharp ice with weak strength, the ice manages to slide away from the platform column. External dynamic models are capable of predicting dissipated energy with reasonable accuracy for both the 3DOF and 6DOF cases. In case of blunt ice with high strength, the ice penetrated into the platform panel with significant structural damage and ice motions were locked to various extents. This *motion locking effect* may decrease significantly the accuracy of the predicted energy dissipation by external dynamic models. This can however be remedied by enforcing *'sticking'* conditions using a large equivalent friction coefficient. *The motion locking effect* widely exists in various collision problems, not only in ice collisions, but also ship collisions.

4. Based on simulation results, an equivalent added mass being the average value of infinite frequency and zero frequency added masses is recommended for practical estimation of the total energy in glacial ice collisions.

Supplementary video related to this article can be found at https://doi.org/10.1016/j.oceaneng.2021.108827

CRediT authorship contribution statement

Zhaolong Yu: Conceptualization, Methodology, Validation, Writing – review & editing. **Jørgen Amdahl:** Conceptualization, Methodology, Supervision, Writing – review & editing, Project administration, Funding acquisition.

Declaration of competing interest

The authors declare that they have no known competing financial interests or personal relationships that could have appeared to influence the work reported in this paper.

Acknowledgments

References

Alsos, H.S., 2008. Ship Grounding: Analysis of Ductile Fracture, Bottom Damage and Hull Girder Response.

Alsos, H.S., Hopperstad, O.S., Törnqvist, R., Amdahl, J., 2008. Analytical and numerical analysis of sheet metal instability using a stress based criterion. Int. J. Solid Struct. 45 (7), 2042–2055.

Amdahl, J., 2019. Impact from ice floes and icebergs on ships and offshore structures in Polar Regions. In: 2nd Computational Methods in Offshore Technology. COTech, 2019.

Bressan, J., Williams, J., 1983. The use of a shear instability criterion to predict local necking in sheet metal deformation. Int. J. Mech. Sci. 25 (3), 155–168.

Calle, M.A., Verleysen, P., Alves, M., 2017. Benchmark study of failure criteria for ship collision modeling using purpose-designed tensile specimen geometries. Mar. Struct. 53, 68–85.

Daley, C., 1994. MSI Ice Loads Data: Compilation of Medium Scale Ice Indentation Test Results and Comparison to ASPPR. Daley R & E.

Das, J., Ehlers, S., 2015. Numerical simulation of crushing and bending failure of ice using SPH. In: International Conference on Offshore Mechanics and Arctic Engineering. American Society of Mechanical Engineers. V008T007A019.

Derradji-Aouat, A., 2000. A Unified Failure Envelope for Isotropic Fresh Water Ice and Iceberg Ice.

Ehlers, S., Broekhuijsen, J., Alsos, H.S., Biehl, F., Tabri, K., 2008. Simulating the collision response of ship side structures: a failure criteria benchmark study. Int. Shipbuild. Prog. 55 (1–2), 127–144.

Fish, A.M., 1991. Creep and Yield Model of Ice under Combined Stress. COLD REGIONS RESEARCH AND ENGINEERING LAB HANOVER NH.

Gagnon, R., 2011. A numerical model of ice crushing using a foam analogue. Cold Reg. Sci. Technol. 65 (3), 335–350.

Gagnon, R., Wang, J., 2012. Numerical simulations of a tanker collision with a bergy bit incorporating hydrodynamics, a validated ice model and damage to the vessel. Cold Reg. Sci. Technol. 81, 26–35.

Han, D., Lee, H., Choung, J., Kim, H., Daley, C., 2017. Cone ice crushing tests and simulations associated with various yield and fracture criteria. Ships Offshore Struct. 12 (Suppl. 1), S88–S99.

Hill, B., 2006. Ship Collision with Iceberg Database.

Hill, R., 1952. On discontinuous plastic states, with special reference to localized necking in thin sheets. J. Mech. Phys. Solid. 1 (1), 19–30.

Huang, L., Tuhkuri, J., Igrec, B., Li, M., Stagonas, D., Toffoli, A., Cardiff, P., Thomas, G., 2020. Ship resistance when operating in floating ice floes: a combined CFD&DEM approach. Mar. Struct. 74, 102817.

Iacs, 2011. Requirements Concerning Polar Class. International Association of Classification Societies London.

Ince, S.T., Kumar, A., Paik, J.K., 2017a. A new constitutive equation on ice materials. Ships Offshore Struct. 12 (5), 610–623.

Ince, S.T., Kumar, A., Park, D.K., Paik, J.K., 2017b. An advanced technology for structural crashworthiness analysis of a ship colliding with an ice-ridge: numerical modelling and experiments. Int. J. Impact Eng. 110, 112–122.

Iso19906, 2010. Petroleum and Natural Gas Industries – Arctic Offshore Structures. International Organization for Standardization.

Iso-19906, 2010. Arctic Offshore Structures Standard.

Kennedy, K.P., 1990. Dynamic Activity and Crushed Ice Behavior in Medium-Scale Ice-Structure Interactions. Memorial University of Newfoundland.

Kierkegaard, H., 1993. Ship Collisions with Icebergs. Danmarks Tekniske Højskole. Instituttet for Skibs-og Havteknik.

Kim, S.J., Kõrgersaar, M., Ahmadi, N., Taimuri, G., Kujala, P., Hirdaris, S., 2021. The influence of fluid structure interaction modelling on the dynamic response of ships subject to collision and grounding. Mar. Struct. 75, 102875.

Le Sourne, H., Besnard, N., Cheylan, C., Buannic, N., 2012. A ship collision analysis program based on upper bound solutions and coupled with a large rotational ship movement analysis tool. J. Appl. Math. 27, 2012.

Liu, Z., Amdahl, J., 2010. A new formulation of the impact mechanics of ship collisions and its application to a ship–iceberg collision. Mar. Struct. 23 (3), 360–384.

Liu, Z., Amdahl, J., 2019. On multi-planar impact mechanics in ship collisions. Mar. Struct. 63, 364–383.

Liu, Z., Amdahl, J., Løset, S., 2011. Plasticity based material modelling of ice and its application to ship–iceberg impacts. Cold Reg. Sci. Technol. 65 (3), 326–334.

Lu, W., Amdahl, J., Lubbad, R., Yu, Z., Løset, S., 2020. Glacial Ice Impacts, Part I: Wave-Driven Motion and Small Glacial Ice Feature Impacts. Submitted to jounal.

Lu, W., Yu, Z., Marnix, V.d.B., Dennis, M., Raed, L., Vegard, H., Amdahl, J., Løset, S., Kim, E., 2019. Loads, Design and Operations of Floaters in the Arctic (Nord ST20). PTIL - LASTER, DESIGN OG OPERASJON AV FLYTERE I NORDOMRÅDENE (NORD ST20) 2019/313.

Lu, W., Yu, Z., Van den Berg, M., Lubbad, R., Amdahl, J., Løset, S., Kim, E., 2018. Assessment of Structural Damage Due to Glacial Ice Impact. PTIL-Konstruksjonssikkerhet I Nordområdene. Petroleumstilsynet, Stavanger.

Marinatos, J., Samuelides, M., 2015. Towards a unified methodology for the simulation of rupture in collision and grounding of ships. Mar. Struct. 42, 1–32.

Motora, S., Fujino, M., Sugiura, M., Sugita, M., 1971. Equivalent added mass of ships in collisions. Selected papers from the journal of the Society of Naval Architects of Japan 7, 138–148.

Ommani, B., Berthelsen, P.A., Lie, H., Aksnes, V., Løland, G., 2019. Hydrodynamic modelling and estimating response of glacial ice near a drilling rig. In: International Conference on Offshore Mechanics and Arctic Engineering. American Society of Mechanical Engineers. V008T007A013.

Pernas-Sánchez, J., Pedroche, D., Varas, D., López-Puente, J., Zaera, R., 2012. Numerical modeling of ice behavior under high velocity impacts. Int. J. Solid Struct. 49 (14), 1919–1927.

Petersen, M.J., 1982. Dynamics of ship collisions. Ocean. Eng. 9 (4), 295–329.

Petersen, M.J., Pedersen, P.T., 1981. Collisions between ships and offshore platforms, offshore technology conference. In: Offshore Technology Conference.

Quinton, B.W., 2008. Progressive Damage to a Ship's Structure Due to Ice Loading. Memorial University of Newfoundland.

Rudan, S., Ćatipović, I., Berg, R., Völkner, S., Prebeg, P., 2019. Numerical study on the consequences of different ship collision modelling techniques. Ships Offshore Struct. 14 (Suppl. 1), 387–400.

Sayeed, T., Colbourne, B., Quinton, B., Molyneux, D., Peng, H., Spencer, D., 2017. A review of iceberg and bergy bit hydrodynamic interaction with offshore structures. Cold Reg. Sci. Technol. 135, 34–50.

Song, M., Kim, E., Amdahl, J., Ma, J., Huang, Y., 2016. A comparative analysis of the fluid-structure interaction method and the constant added mass method for ice-structure collisions. Mar. Struct. 49, 58–75.

Storheim, M., Amdahl, J., Martens, I., 2015. On the accuracy of fracture estimation in collision analysis of ship and offshore structures. Mar. Struct. 44, 254–287.

Tavakoli, M.T., Amdahl, J., 2010. Analysis of Collision between Midgard Platform and 8000 Tonnes Displacement Ship.

Timco, G.W., Weeks, W.F., 2010. A review of the engineering properties of sea ice. Cold Reg. Sci. Technol. 60 (2), 107–129.

Tørnqvist, R., 2003. Design of Crashworthy Ship Structures. Technical University of Denmark, Kgns Lyngby, Denmark.

Yu, Z., Amdahl, J., 2016. Full six degrees of freedom coupled dynamic simulation of ship collision and grounding accidents. Mar. Struct. 47, 1–22.

Yu, Z., Amdahl, J., 2018. A review of structural responses and design of offshore tubular structures subjected to ship impacts. Ocean. Eng. 154, 177–203.

Yu, Z., Amdahl, J., Greco, M., Xu, H., 2019a. Hydro-plastic response of beams and stiffened panels subjected to extreme water slamming at small impact angles, part II: numerical verification and analysis. Mar. Struct. 65, 114–133.

Yu, Z., Amdahl, J., Kristiansen, D., Bore, P.T., 2019b. Numerical analysis of local and global responses of an offshore fish farm subjected to ship impacts. Ocean. Eng. 194, 106653.

Yu, Z., Liu, Z., Amdahl, J., 2019c. Discussion of assumptions behind the external dynamic models in ship collisions and groundings. Ships Offshore Struct. 14 (sup1), 45–62.

Yu, Z., Lu, W., Van den Berg, M., Amdahl, J., Løset, S., 2020. Glacial Ice Impacts, Part II: Damage Assessment and Ice-Structure Interactions in Accidental Limit States (ALS). Submitted to jounal.

Yu, Z., Shen, Y., Amdahl, J., Greco, M., 2016. Implementation of linear potential-flow theory in the 6DOF coupled simulation of ship collision and grounding accidents. J. Ship Res. 60 (3), 119–144.